



# Selective potassium uptake via biocompatible zeolite–polymer hybrid microbeads as promising binders for hyperkalemia

Zhoujun Wang<sup>a</sup>, Wei Sun<sup>b</sup>, Zhiwei Wei<sup>a</sup>, Jianxu Bao<sup>a</sup>, Xin Song<sup>a</sup>, Yupei Li<sup>c,d</sup>, Haifeng Ji<sup>a</sup>, Jue Zhang<sup>a</sup>, Chao He<sup>a</sup>, Baihai Su<sup>c,d</sup>, Weifeng Zhao<sup>a,\*</sup>, Changsheng Zhao<sup>a,e,f</sup>

<sup>a</sup> College of Polymer Science and Engineering, State Key Laboratory of Polymer Materials Engineering, Sichuan University, Chengdu, 610065, China

<sup>b</sup> Laboratory Department of General Hospital of Western Theatek Command, Chengdu, 610000, China

<sup>c</sup> Department of Nephrology, West China Hospital, Sichuan University, Chengdu, 610041, China

<sup>d</sup> Institute for Disaster Management and Reconstruction, Sichuan University, Chengdu, 610207, China

<sup>e</sup> College of Chemical Engineering, Sichuan University, Chengdu, 610065, China

<sup>f</sup> College of Biomedical Engineering, Sichuan University, Chengdu, 610064, China

## ARTICLE INFO

### Keywords:

Potassium uptake  
Competitive adsorption  
Microbead  
Zeolite  
Blood compatibility

## ABSTRACT

Patients with chronic kidney disease are at high risk of hyperkalemia that is associated with various life-threatening complications. Treatments primarily rely on orally administered potassium binding agents, along with low curative effects and various side effects. Herein, direct serum potassium uptake was realized via zeolite–heparin-mimicking-polymer hybrid microbeads. The preparation process involved the synthesis of the heparin-mimicking polymer via the *in situ* cross-linking polymerization of acrylic acid and *N*-vinylpyrrolidone in polyethersulfone solution, the fabrication of microbeads via zeolite-mixing, electro-spraying and phase-inversion, and the subsequent aqueous-phase modifications based on ion-exchange and metal-leaching. An ultra-high (about 88%) amount of zeolite could be incorporated and well locked inside the polymer matrix. Potassium uptake capability was verified in water, normal saline and human serum, showing high selectivity and fast adsorption. The microbeads exhibited satisfying blood compatibility, negligible hemolysis ratio, prolonged clotting time, inhibited contact activation, and enhanced antifouling property toward serum proteins and cells. The proposed approach toward zeolite–heparin-mimicking-polymer hybrid microbeads provided a cheap, efficient and safe treatment protocol of hyperkalemia for the high-risk patients.

## 1. Introduction

Hyperkalemia is a potentially serious medical condition where the serum potassium level exceeds 5 mmol/L [1]. Due to the pivotal role of kidneys in potassium homeostasis, patients with chronic kidney disease are predisposed to develop this electrolyte disorder that, should it occur, would lead to more severe consequences [2]. This disease is associated with markedly increased mortality, lethal cardiac arrhythmias and a limitation on the use of renin–angiotensin–aldosterone system inhibitors as the essential medications for cardiovascular and kidney disease [3,4]. Excess serum potassium can be removed by redistribution into cells, elimination through the kidney or gastrointestinal tract, and extracorporeal blood purification [5]. In blood purification, traditional hemodialysis remains the definitive strategy, which is based on ionic diffusion driven by the transmembrane

potassium gradient between serum and low-potassium dialysate [6,7]. Wearable artificial kidneys (WAK) obviate the dependency on stationary hemodialysis machines and mitigate the burden of daily life, but are encumbered with the issue of dialysate regeneration [8]. Hemoperfusion provides fast removal of uremic toxins via adsorbents, while the primary challenge is to discover satisfied selective binding agents for serum potassium uptake.

Specific ion-exchange/detection/storage ability has been verified in various agents, including zeolites [9–11], sodium zirconium cyclosilicate [12], layered phosphates [13,14], carbon-based materials [15,16], polymer-based materials [17,18], crown ethers [19,20] and their graphene derivatives [21,22]. Among them, zeolites are considered as the main trial materials in consideration of production cost and specific binding ability. The interconnected micropores in these crystalline aluminosilicates accommodate exchangeable cations that compensate

Peer review under responsibility of KeAi Communications Co., Ltd.

\* Corresponding author.

E-mail address: [weifeng@scu.edu.cn](mailto:weifeng@scu.edu.cn) (W. Zhao).

<https://doi.org/10.1016/j.bioactmat.2020.08.032>

Received 7 July 2020; Received in revised form 19 August 2020; Accepted 24 August 2020

2452-199X/ © 2020 The Authors. Publishing services by Elsevier B.V. on behalf of KeAi Communications Co., Ltd. This is an open access article under the CC BY-NC-ND license (<http://creativecommons.org/licenses/by-nc-nd/4.0/>).

negative charges of the framework [23,24]. However, the active sites are mostly located inside the microporous solids of zeolites, and the limitation of open surface areas restricts the mass transport of ions via channels and cages, especially when applied in blood that is full of biomacromolecules. Therefore, creating new pathways (i.e., mesoporosity) is beneficial for ion binding, which is achieved by template/reaction-based synthesis of new zeolites, or dealumination/desilication-based metal-leaching of ready-made zeolites [25,26].

Powdered zeolites show inescapable limitations when applied as blood-contacting materials for the inevitable leakage of microparticles, resulting in the failure of blood purification. Zeolites are preferable to be processed into polymer–zeolite composites for better blood compatibility, such as hybrid microbeads [27,28]. Polyethersulfone (PES) has been proved to be a suitable carrier of particles in microbeads for its ideal mechanical and chemical stability [29]. Utilization of biomolecules (e.g., surface heparinization, nitric oxide delivery) may provide ideal biocompatibility for heart stents, blood vessels and other blood-contacting materials [30,31]. Heparin-mimicking polymers show good blood compatibility and anticoagulation effect, as the promising alternatives to heparin in blood purification [32,33]. These polymers could benefit the treatment of hyperkalemia, as heparin *per se* is a risk factor for hyperkalemia due to the interference with renal potassium excretion [4,34]. Therefore, we hypothesized that an adsorbent comprising metal-leached zeolite, PES and heparin-mimicking polymer could gather their advantages of specific potassium binding ability, mechanical stability and blood compatibility.

Herein, a commercially-available super-hydrophilic LTA-type zeolite was selected from six binding agents. The preparation process included the synthesis of the heparin-mimicking polymer via the *in situ* cross-linking polymerization of acrylic acid (AA) and *N*-vinylpyrrolidone (NVP) in the PES solution; the preparation of microbeads via zeolite-mixing, electro-spraying and phase-inversion; and the subsequent aqueous-phase modifications based on ion-exchange and metal-leaching. The physicochemical properties were systematically characterized, including morphologies, chemical structures, elemental compositions, water contact angles (WCAs) and zeta potentials (ZPs). Potassium uptake capability was verified in water, normal saline and human serum. The effects of composition, zeolite amount, modification method and adsorbent dosage on potassium uptake were studied. The pseudo-first-order kinetic model, the pseudo-second-order kinetic model and the intraparticle diffusion model were applied to study the adsorption kinetics, while the Freundlich and the Langmuir models were applied to study the adsorption isotherms. The blood compatibility was also evaluated, including protein adsorption, blood routine, blood cell adhesion, hemolysis, clotting time, complement activation and contact activation.

## 2. Materials and methods

### 2.1. Materials

Polyethersulfone (PES,  $M_w = 58$  k, Ultrason E 6020P, more details are shown in Table S1) was obtained from BASF. Acrylic acid (AA), *N*-vinylpyrrolidone (NVP), 2,2'-azobis (2-methylpropionitrile) (AIBN), *N,N'*-methylene bis(acrylamide) (MBA), potassium chloride (KCl), sodium hydroxide (NaOH), sodium chloride (NaCl), ammonium chloride ( $\text{NH}_4\text{Cl}$ ) and ethylenediaminetetraacetic acid disodium salt dihydrate ( $\text{EDTA-Na}_2$ ) were purchased from Aladdin. *N,N*-dimethylacetamide (DMAc), ethanol ( $\text{C}_2\text{H}_5\text{OH}$ ) and normal saline (0.9% NaCl) were ordered from Chengdu Chron Chemicals. Bovine serum albumin (BSA) and bovine serum fibrinogen (BFG) were received from Sigma. Zeolite LTA and mordenite were obtained from Shanghai Saint Chemical New Material. Zeolite Y was ordered from Alfa. Clinoptilolite was received from Guotoushengshi Science & Technology. Permutit was received from Aladdin. Zirconium phosphate (ZrP) was received from Chengdu Huaxia Chemical Reagent. The natural zeolites (clinoptilolite and

mordenite) were sourced from China and sifted through a 1000-mesh steel sieve before use.

### 2.2. Evaluation of binding agents for microbeads

Scanning electron microscopy (SEM) and energy dispersive spectra (EDS) were obtained using a JMS-7500F SEM. Thermogravimetric analysis (TGA) was conducted on a TGA/DSC 3+ thermogravimetric analyzer at a heating rate of  $10^\circ\text{C}/\text{min}$ . X-ray diffraction (XRD) patterns were obtained using a PANalytical X'Pert Pro Multipurpose Diffractometer DY129 with Ni-filtered  $\text{CuK}\alpha$  X-ray radiation ( $\lambda = 1.5418 \text{ \AA}$ ,  $K\alpha_1 = 1.5405 \text{ \AA}$ ,  $K\alpha_2 = 1.5444 \text{ \AA}$ ,  $K\alpha_2/K\alpha_1 = 0.5$ ). X-ray photoelectron spectroscopy (XPS) was performed with an XSAM800 electron spectrometer. X-ray fluorescence (XRF) analysis was conducted using an XRF-1800. The amounts of heavy metal were tested by a sulfuric acid digestion method according to ASTM D7442 using a 5100 SVDV-ICP-OES. The potassium uptake and the  $\text{Na}^+$  fluctuation were measured by the static adsorption tests. For the protein adsorption test, the hybrid microbeads that corresponded to the binding agents were prepared via manual-injection and phase-inversion, following the formula for the microbeads  $\text{PHZ}_4$ , as shown in Table S2. The details are shown in Supporting Information.

### 2.3. Preparation of the hybrid microbeads

The heparin-mimicking polymer was synthesized via the *in situ* cross-linking polymerization of two monomers (AA and NVP) in the presence of AIBN as initiator and MBA as cross-linker in PES/DMAc solution. The hybrid suspensions were obtained by adding zeolite LTA powder into the polymer solution with mechanical agitation and ultrasonic dispersion. The microbeads were prepared from the suspensions via electro-spraying and phase-inversion. The major formulas for the suspensions to prepare the corresponding microbeads are listed in Table 1 and detailed in Table S2, including pristine PES microbeads (P), heparin-mimicking polymer PES–P (AA–NVP) microbeads (PH), zeolite–PES hybrid microbeads ( $\text{PZ}_n$ ), and zeolite–PES–P (AA–NVP) hybrid microbeads with different added amounts of zeolite ( $\text{PHZ}_n$ ), in which  $n$  represents zeolite had  $n$  times the mass of PES in the suspension.

### 2.4. Aqueous-phase modifications

The hybrid microbeads  $\text{PHZ}_4$  were further modified with different methods, each of which included one or several processes. As summarized in Table 2, the processes were the heating treatments for ion-exchange in  $\text{NH}_4\text{Cl}$  or NaCl solution, and those for metal-leaching in  $\text{EDTA-Na}_2$  or NaOH solution. A combined method was applied to obtain the microbeads  $\text{PHZ}_4\text{-NH}_4\text{-Acid-Base-Na}$ , which was abbreviated as  $\text{PHZ}_4\text{-x}$ . The details are shown in Supporting Information.

### 2.5. Characterization of the hybrid microbeads

An Apreo S HiVac scanning electron microscope was used for SEM and EDS analysis of the lyophilized and sectioned microbeads. EDX mapping analysis was conducted on  $\text{PHZ}_4\text{-x}$  that had a quick contact (15 min) with KCl solution, then rinsed and lyophilized. Atomic force microscopy (AFM) was performed on a CP II atomic force microscope.

**Table 1**  
The formulas for the suspensions.

Sample	DMAc/g	PES/g	AA/g	NVP/g	zeolite/g
P	92	8	0	0	0
PH	92	8	1.2	0.4	0
$\text{PZ}_4$	92	8	0	0	32
$\text{PHZ}_4$	92	8	1.2	0.4	32

**Table 2**  
Treatments in aqueous-phase modifications.

Code	Reagent	Conc./M	Temp./°C	Time/h
-DI	\	\	60	6
-NH4	NH <sub>4</sub> Cl	4	60	<sup>a</sup> 2*3
-Na	NaCl	4	60	<sup>b</sup> 2*3
-Acid	EDTA-Na <sub>2</sub>	0.2	70	6
-Base	NaOH	4	70	1
-Base2	NaOH	0.2	70	1

<sup>a</sup> Repeat 3 times, 2 h for each.

<sup>b</sup> Repeat 3 times, 2 h for each.

Nitrogen adsorption isotherms were measured with an ASAP 2020 sorption analyzer, and the pore-size distribution data were obtained by the Barrett–Joiner–Halenda (BJH) model. XRD patterns were obtained using a PANalytical X'Pert Pro multipurpose diffractometer DY129. XPS was performed with an XSAM800 electron spectrometer. Fourier transform infrared spectroscopy (FTIR) was performed with a Nicolet 560 spectrometer. TGA was proceeded using a TGA/DSC 3+ thermogravimetric analyzer at a heating rate of 10 °C/min. The spin-casting membranes that corresponded to the microbeads were prepared for the tests of ZPs and WCAs. The ZPs were measured using the “EKA” Electro Kinetic Analyzer, and the WCAs were measured using an optical tensiometer Theta T200. For the test of mechanical property, three microbeads of PHZ<sub>4</sub>-x were placed between two glass plates; the weight bars were placed on the upper glass plate to see if there was any deformation of the microbeads. The details are shown in Supporting Information.

## 2.6. Potassium uptake

A certain amount of adsorbents were rehydrated in plastic centrifuge tubes in triplicate before the contact with adsorbates at the dosage of 5 mg/mL in an incubator at 37 °C for 2 h. The KCl solution in deionized water (initial states: pH = 7.2, K<sup>+</sup> = 10 mmol/L, Na<sup>+</sup> = 0) was named as the DI group. The solution of KCl in normal saline was set as the NS group to study the uptake under the major ion competition (initial states: pH = 7.2, K<sup>+</sup> = 10 mmol/L, Na<sup>+</sup> = 150 mmol/L). The concentrations of K<sup>+</sup> and Na<sup>+</sup> in the supernatants were measured by atomic absorption spectrometry (AAS). The K<sup>+</sup> uptake and the Na<sup>+</sup> fluctuation were calculated by Equation (1); for the binding agents, the selectivity of K<sup>+</sup> over Na<sup>+</sup> was calculated by Equations (2)–(3), where c<sub>0</sub> (mmol/L) and c<sub>e</sub> (mmol/L) are the initial concentration and the equilibrium concentration of metal ions; m (g) is the weight of the adsorbent; V (L) is the volume of the solution; K<sub>d</sub> is the thermodynamic equilibrium constant (L/g); S<sub>K/Na</sub> is the cation selectivity ratio of potassium over sodium ions [35].

$$q_e = (c_0 - c_e) / m \times V \quad (1)$$

$$K_d = q_e / c_e \quad (2)$$

$$S_{K/Na} = K_{d,K} / K_{d,Na} = \frac{c_{0,K} - c_{e,K}}{c_{e,K}} / \frac{c_{0,Na} - c_{e,Na}}{c_{e,Na}} \quad (3)$$

The effects of composition, zeolite amount, modification method and adsorbent dosage on potassium uptake were studied by static adsorption tests. The adsorption kinetics and isotherms were also investigated. Static adsorption tests and column filtration tests were conducted to study the K<sup>+</sup> uptake in human serum. The details are shown in Supporting Information.

## 2.7. Blood compatibility

Two types of proteins (BSA and BFG) were involved in the protein adsorption tests, and the adsorption amount was determined by the Micro BCA Protein Assay Kit. Whole blood was donated by male

volunteers and collected from the West China Hospital of Sichuan University. In the blood routine test, whole blood after the contact with samples was tested by using a BC-5310 auto hematology analyzer. The blood was centrifuged to obtain platelet-poor plasma (PPP), platelet-rich plasma (PRP) and red blood cells (RBCs). PPP was used for the clotting time tests, where activated partial thromboplastin time (APTT), thrombin time (TT) and prothrombin time (PT) were tested by using a CA-50 blood coagulation analyzer. In the platelet adhesion test, PRP was incubated with the samples, then immobilized and dehydrated; the adhered platelets (PLTs) were observed by using an Apreo S HiVac SEM. In the hemolysis test, RBCs were incubated with the samples; the absorbance in the suspensions was measured using a UV-1750 UV-vis spectrometer, and the hemolysis ratio was calculated by Equation S(2); the RBCs sampled from the suspensions were observed under an Olympus IX53 microscope. Complement activation, contact activation and platelet activation were evaluated by an enzyme-linked immune sorbent assay with Human Complement Fragment 3a (C3a) kit, Human Complement Fragment 5a (C5a) kit (BD Biosciences), thrombin-antithrombin III (TAT) kit (Assaypro LLC) and Human Platelet Factor 4 (PF4) kit (Hyphen BioMed). The details are shown in the Supporting Information.

## 3. Results and discussions

### 3.1. Evaluation of binding agents for microbeads

Six candidates as the binding agents for microbeads were involved in the evaluation, including two synthetic zeolitic agents (zeolite LTA and zeolite Y), two natural zeolitic agents (mordenite and clinoptilolite) and two synthetic non-zeolitic agents (permutit and ZrP). The SEM images (Fig. 1A) show the morphology of the powdered agents: the cubic structure of zeolite LTA was more regular in shape and more uniform in size, compared with the block or lamellar structures with inhomogeneity in other agents. The XRD patterns in 5–45° (2θ) (Fig. 1B) were obtained and fitted with standard XRD data (JCPDS); the synthetic agents generally had higher phase purity than the natural ones (mordenite and clinoptilolite). In addition, the pattern of zeolite LTA in a broader range of 5–80° (2θ) is shown in Fig. S1. As indicated by the curves of TGA (Fig. 1C) and differential thermogravimetry (DTG) (Fig. S2), all the agents (pre-dried at 70 °C) were thermally stable. The EDS spectra and elemental fractions are shown in Fig. S3 for elemental analysis. Besides, the XPS and the XRF results of zeolite LTA are shown in Fig. S4 and Table S3. The absence of heavy metal content in zeolite LTA was confirmed by the method of sulfuric acid digestion and ICP-OES analysis, according to ASTM D7442.

The adsorption performance of the six powdered agents was evaluated for the selection of the best binding agent. Since in human blood, the concentrations of Na<sup>+</sup> and K<sup>+</sup> are the highest among all the cations, while the concentration of Na<sup>+</sup> (135–145 mmol/L) is dozens of times higher than that of K<sup>+</sup> (3.5–5.5 mmol/L). Therefore, the ion competition from Na<sup>+</sup> was a primary concern in the following adsorption tests. The K<sup>+</sup> uptake, the Na<sup>+</sup> fluctuation and the K<sup>+</sup>/Na<sup>+</sup> selectivity of the powdered agents were evaluated, as shown in Fig. 1D. Zeolite LTA and clinoptilolite exhibited excellent K<sup>+</sup> uptake without causing obvious Na<sup>+</sup> fluctuation, while other agents had either low K<sup>+</sup> uptake (mordenite and ZrP) or high Na<sup>+</sup> fluctuation (zeolite Y and permutit). In addition, zeolite LTA was preferable for its higher K<sup>+</sup>/Na<sup>+</sup> selectivity.

Then, manual-injected hybrid beads were prepared following the formula for PHZ<sub>4</sub> for the further evaluation of the binding agents, as shown in Fig. 1E. High amounts of binding agents were added into suspensions to meet the expectation of ideal K<sup>+</sup> uptake. The suspensions for zeolite LTA and clinoptilolite showed excellent stability and good feasibility for processing, while other agents were either easy to precipitate in suspensions and hard to be extruded by syringes, or unable to maintain the spherical shape during phase-inversion. The anti-fouling property of the hybrid beads was compared in protein

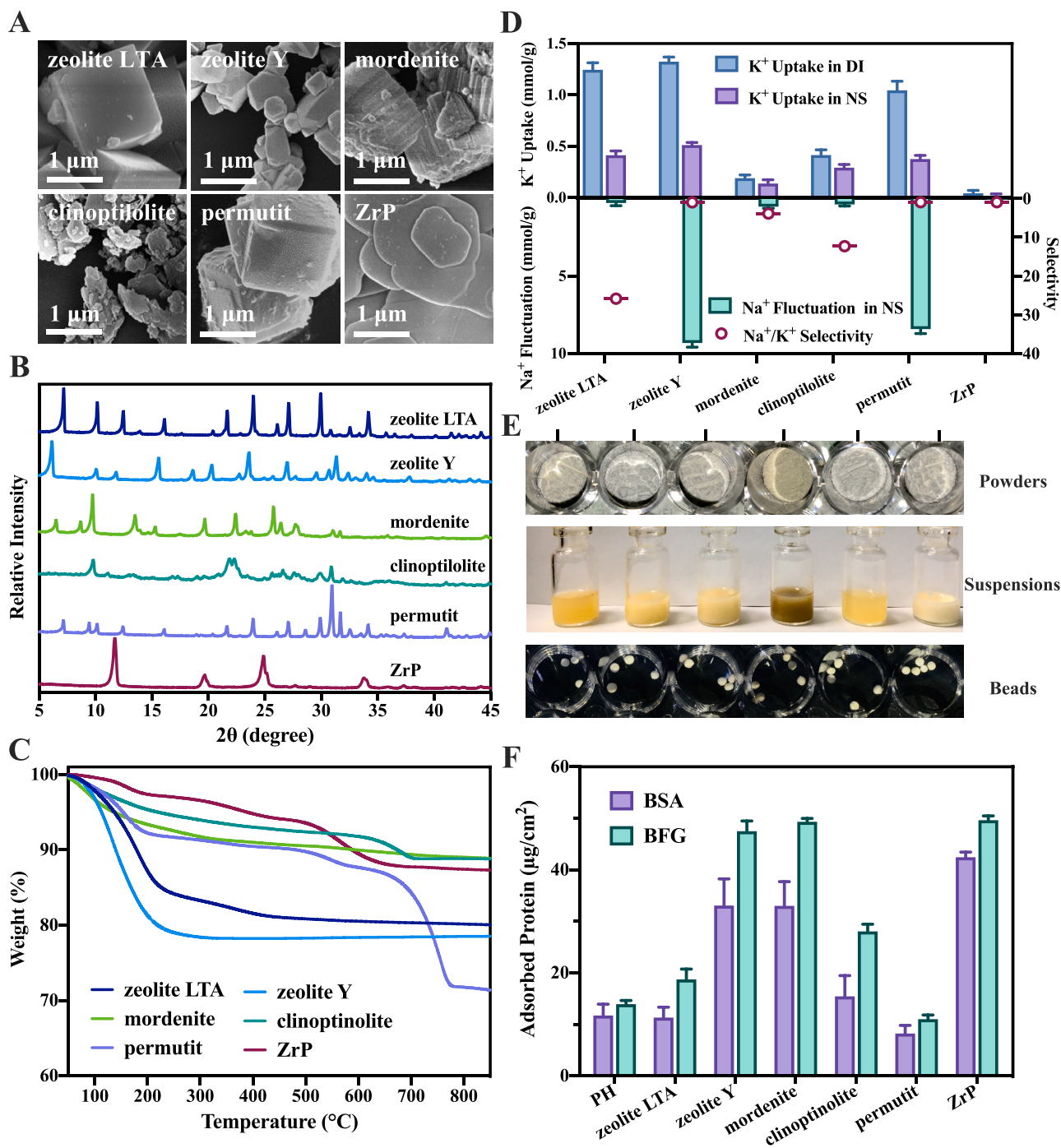


Fig. 1. (A) SEM images, (B) XRD patterns and (C) TGA curves of the binding agents. (D) K<sup>+</sup> uptake, Na<sup>+</sup> fluctuation and K<sup>+</sup>/Na<sup>+</sup> selectivity of the binding agents. The results were expressed as means  $\pm$  SD, n = 3. (E) Photographs of the powders, hybrid suspensions and manually-injected beads of the binding agents. (F) Protein adsorption amounts of the manually-injected beads. The results were expressed as means  $\pm$  SD, n = 6.

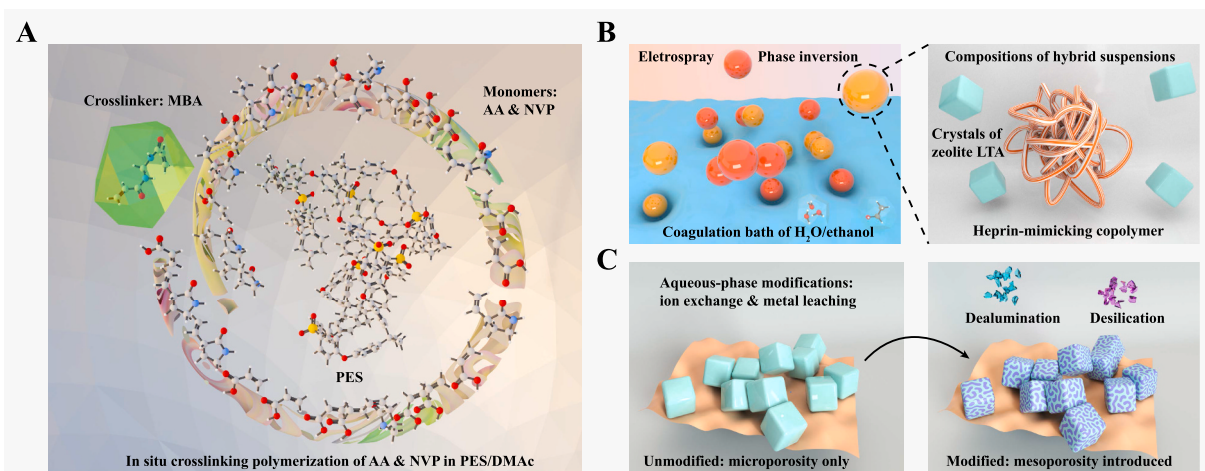
adsorption tests, in which the hybrid beads of zeolite LTA and permutit exhibited the lowest adsorption amounts of BSA and BFG (Fig. 1F).

In sum, zeolite LTA was chosen as the binding agent for preparing the microbeads, because of the preferable morphology, higher K<sup>+</sup> uptake and selectivity, good miscibility with the polymer, as well as thermal stability, phase purity and antifouling property.

### 3.2. Preparation of hybrid microbeads

The heparin-mimicking polymer was synthesized via the *in situ* cross-linking polymerization (Scheme 1A) of acrylic acid (AA) and N-

vinylpyrrolidone (NVP) in PES solution. Herein, PES played three roles: (i) as the scaffold that guided the formation and entanglement of the hydrophilic polymer chains during polymerization, (ii) as the hydrophobic part that ensured fast phase-inversion to maintain sphericity in the coagulation bath, (iii) and as the framework of linear-chain-polymer to provide mechanical support for the microbeads. The blood compatibility of the super-hydrophilic zeolite LTA powder was expected to be improved by the heparin-mimicking polymer, in which poly (acrylic acid) (PAA) introduced carboxyl groups and polyvinylpyrrolidone (PVP) enhanced the miscibility between PES and the copolymer [36]. A certain amount of zeolite powder was added in the



**Scheme 1.** (A) *In situ* cross-linking polymerization of AA and NVP in PES/DMAc solution with MBA as cross-linker. (B) Preparation of microbeads from electro-sprayed droplets of the hybrid suspensions comprising zeolite LTA particles and heparin-mimicking polymer via phase-inversion in the coagulation bath of water and ethanol. (C) Aqueous-phase modifications based on ion-exchange and metal-leaching to introduce mesoporosity to the microporous zeolite LTA in the microbeads.

as-prepared polymer solution, following mechanical agitation and supersonic dispersion under vacuum, to obtain the hybrid suspension. The hybrid suspension was extruded by a syringe using an electrospinning machine. The added zeolite, as the solid anion cluster with charged-balanced cations, facilitated the action of electric field force and the formation of uniform droplets. The microbeads of about 600  $\mu\text{m}$  in diameter with narrow distribution were fabricated via phase-inversion in the coagulation bath of water and ethanol (Scheme 1B).

The differences between the suspensions and microbeads of PZ<sub>4</sub> and PHZ<sub>4</sub> were revealed in terms of the stability of suspensions and the miscibility of two phases (zeolite–polymer). Distinct layers appeared in the suspension for PZ<sub>4</sub> without any operation for 60 min, while the suspension for PHZ<sub>4</sub> remained homogeneous without precipitation (Fig. 2A). The zeolite particles were rarely exposed on the surface of PHZ<sub>4</sub> and were generally covered with the polymer phase with better consistency and fewer defects (Fig. 2B). Researches showed that the cationic zeolite LTA of a low Si/Al ratio was highly hydrophilic, with interfacial water covered in the crystalline surface along with the hydrogen-bonded water confined in the channels and cages [37,38]. Besides, the crystalline surface imposed a significant interaction of ordering with adjacent water and influencing the water diffusion [39]. Therefore, the interactions should be ascribed to the hydrogen bonding of the water molecules in zeolite and the carboxyl groups in PAA, thus stabilizing the hybrid suspension even with an ultra-high amount of zeolite, and enhancing the miscibility of the two phases in PHZ<sub>4</sub>.

The interactions of hydrogen-bonding were further investigated by the temperature-dependent two-dimensional infrared (2D IR) analysis for the microbeads during the heating process of 30–140 °C. Fig. 2C shows the 3D views of the 2D IR spectra in 2900–3850  $\text{cm}^{-1}$ . The strong auto-peaks in the synchronous spectra were attributed to the stretching vibration of  $-\text{COO}^-$  of carboxylate groups in the copolymer (near 3550  $\text{cm}^{-1}$  in PH) and that of  $-\text{OH}$  of water molecules in zeolite LTA (near 3250  $\text{cm}^{-1}$  in PZ<sub>4</sub>, or 3300  $\text{cm}^{-1}$  in PHZ<sub>4</sub>). In the asynchronous spectrum of PHZ<sub>4</sub>, two pairs of strong cross-peaks appeared rather than the one in that of PZ<sub>4</sub>; this change at high wavenumbers indicated the strong interactions between two phases. Fig. 2D shows the asynchronous 2D IR spectra of PHZ<sub>4</sub> in the region of 1550–1700  $\text{cm}^{-1}$  that covered the frequency range of the stretching vibration of  $\text{C}=\text{O}$  of carboxylate groups and that of the bending vibration of  $-\text{OH}$  in water molecules. The various pairs of cross-peaks arose from the hydrogen-bond exchange among different configurations of water molecules and the  $\text{C}=\text{O}$  in carboxylate groups. Besides, a set of cross-peaks (near 3300  $\text{cm}^{-1}$ ) and another set (near 3700  $\text{cm}^{-1}$ ) with lower intensity appeared in the synchronous 2D IR spectra of PHZ<sub>4</sub> in 1550–1700  $\text{cm}^{-1}$

vs. 2900–3850  $\text{cm}^{-1}$  (Fig. 2E), which also reflected the strong hydrogen-bonding that endowed PHZ<sub>4</sub> with ideal stability of suspensions and the good miscibility of two phases.

### 3.3. Characterization of the microbeads

The SEM images in Fig. 3A show the cross-sections of the microbeads. The porous structure of PH changed obviously as the addition of zeolite LTA in PHZ<sub>4</sub>: many cubic particles of about 1  $\mu\text{m}$  were distributed among the polymer matrix; the outermost polymer shell became thinner; the thick pore walls changed from a laminar structure into a spongy-bone-like structure with interconnected nodes forming a radial network. These changes endowed PHZ<sub>4</sub> with higher porosity and better contact with aqueous solutions. PHZ<sub>4</sub> was treated with aqueous-phase modifications of ion-exchange, dealumination and desilication to obtain PHZ<sub>4-x</sub>, in which the zeolite was introduced mesoporosity (Scheme 1C). Fig. 3B shows the EDX mapping of PHZ<sub>4-x</sub> that was ever treated with the KCl solution (15 min contact). The fewer lightspots of element Si in the outer surface indicated few zeolite particles located on the surface than in the interior of the microbeads. The well-dispersed S and Si indicated an even zeolite distribution among the polymer matrix. The distribution of element K in the cross-section did not vary along the radial direction, showing good accessibility of the innermost zeolite particles toward  $\text{K}^+$  in the solution. The AFM images (Fig. 3C) display the micromorphology of the polymer shell of PHZ<sub>4-x</sub>, exhibiting sub-micron-sized holes, smaller bulges and irregular defects. The size distributions of mesopores before and after modifications were obtained by nitrogen adsorption at 77 K using the BJH model [40]. In Fig. 3D, the mesopores induced by dealumination and desilication appeared in a broad range of 10–50 nm, which were consistent with the results in other reports [25,41]. The XRD patterns of PHZ<sub>4</sub> and its modified analogs for phase analysis are shown in Fig. S5. The characteristic peaks associated with the zeolite LTA still existed in the patterns of the microbeads, albeit with lower intensities due to the interference of the polymer phase. Some peaks were broadened in the patterns of the modified microbeads, especially PHZ<sub>4-x</sub>, indicating the amorphization of zeolite during modifications. According to the structural characterizations above, the schematic drawings in Fig. 3E depict the multi-layered structure of the hybrid microbeads with hierarchical porosity, where the zeolite particles were evenly dispersed among the polymer matrix. The outermost polymer shell (Fig. 2B) was assumed to allow  $\text{K}^+$  to pass while blocking the much larger proteins and cells in the serum.

For FTIR analysis (Fig. 4A), the appearance of new peaks in the microbeads PH compared to P indicated the successful introduction of

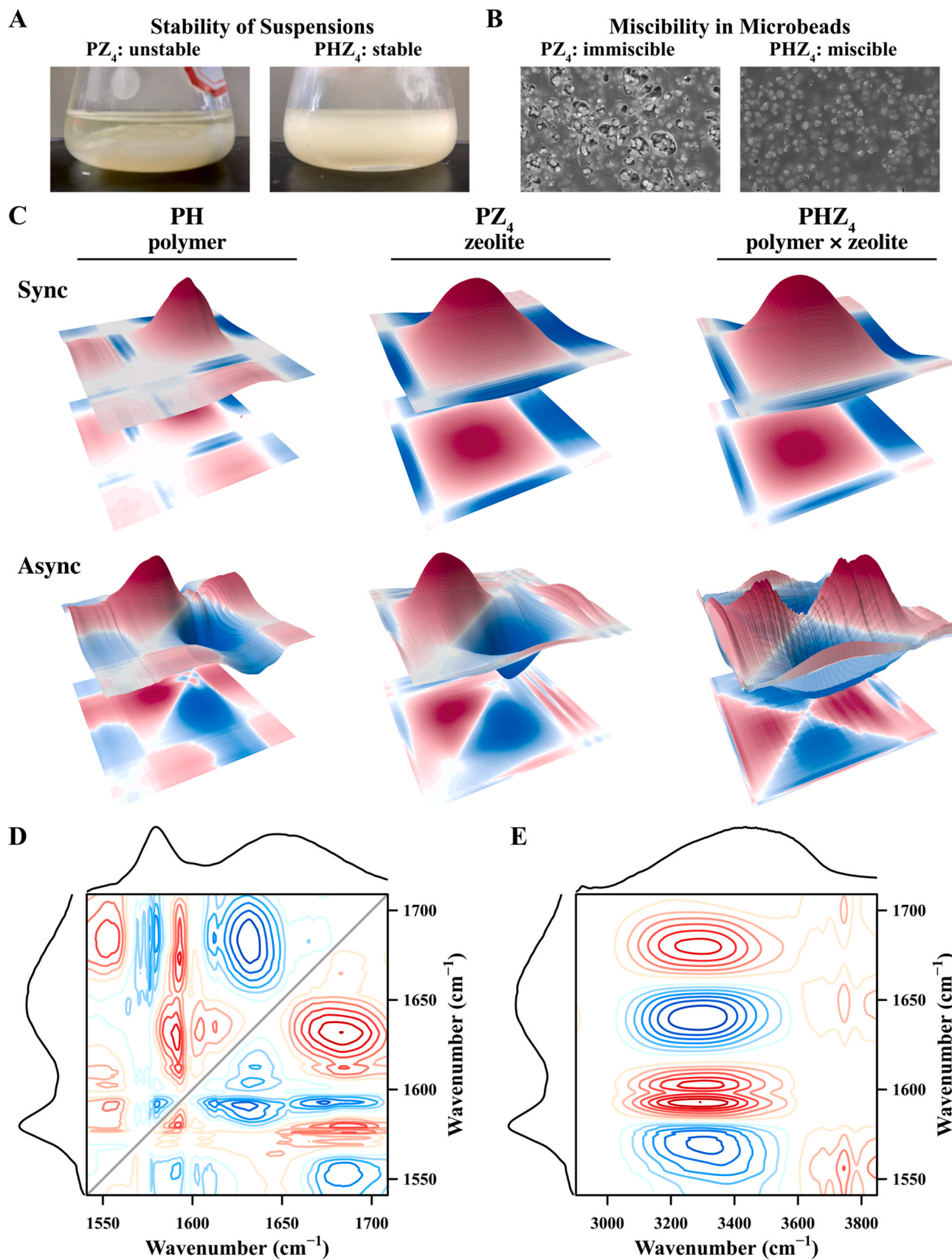
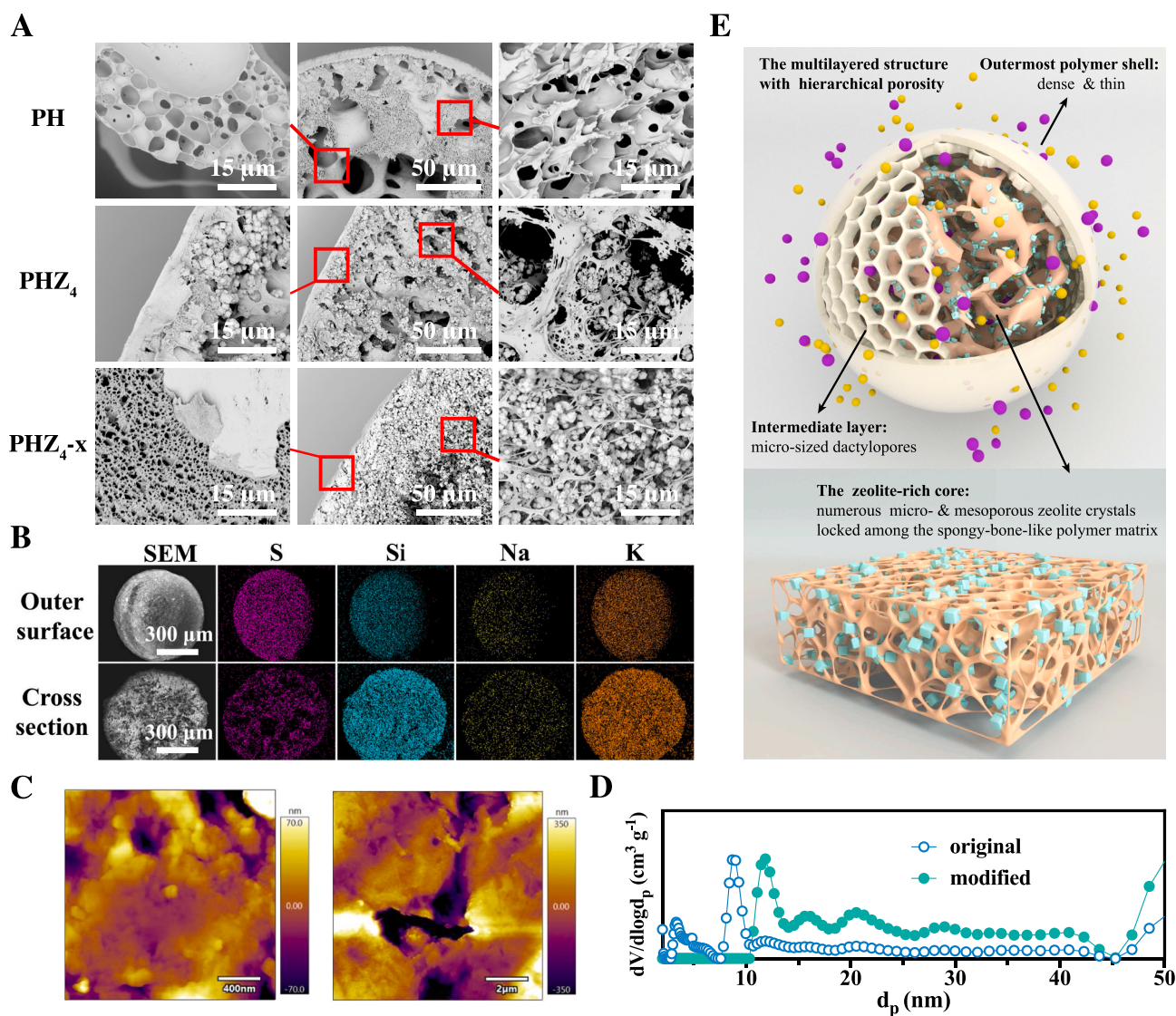


Fig. 2. (A) Stability of the suspensions for PZ<sub>4</sub> and PHZ<sub>4</sub>. (B) Surface SEM images of PZ<sub>4</sub> and PHZ<sub>4</sub>. (C) 3D views of the synchronous and asynchronous 2D IR spectra of PH, PZ<sub>4</sub> and PHZ<sub>4</sub> in the region of 2900–3850 cm<sup>-1</sup>. (D) 2D IR spectra of PHZ<sub>4</sub> in the region of 1550–1700 cm<sup>-1</sup> vs. 1550–1700 cm<sup>-1</sup> and (E) 1550–1700 cm<sup>-1</sup> vs. 2900–3850 cm<sup>-1</sup> with linear FTIR spectra.



**Fig. 3.** (A) SEM images of cross-sections of PH and PHZ<sub>4</sub>. (B) EDX mapping of PHZ<sub>4</sub>-x ever treated with the KCl solution. (C) AFM images of the surface of PHZ<sub>4</sub>-x. (D) BJH pore-size distributions of the original and the modified zeolite LTA. (E) Schematic drawings of the hybrid microbeads showing a multilayered structure with hierarchical porosity.

AA and NVP: the peak at 1720 cm<sup>-1</sup> and the wide peak near 3420 cm<sup>-1</sup> were due to the stretching vibrations of C=O and -OH groups from AA respectively, and the peak at 1640 cm<sup>-1</sup> was due to the C=O groups from NVP [42]. Zeolitic peaks appeared in the spectra of PHZ<sub>4</sub> and PHZ<sub>4</sub>-x: the strong peak near 1000 cm<sup>-1</sup> was due to the stretching vibrations of Si-O-Al and Si-O-Si in the [SiO<sub>4</sub>] and [AlO<sub>4</sub>] tetrahedra of zeolite, and a broad peak of zeolitic hydroxyls in the range of 3500–3800 cm<sup>-1</sup> was associated with Si-OH, Si-O<sub>1</sub>H-Al and Si-O<sub>3</sub>H-Al [43]. PHZ<sub>4</sub>-x shared high similarity with PHZ<sub>4</sub>, albeit with less-intensive zeolitic peaks due to amorphization [44]. EDS and XPS were conducted for elemental analysis. A noticeable level of element N was detected in PHZ<sub>4</sub>, due to the presence of PVP and the cross-linker MBA, while being absent in PZ<sub>4</sub>, as illustrated by the EDS results in Fig. 4B and C. The elemental fractions were listed in the inserted tables, showing considerable amounts of Si and Al. The wide scans of XPS in Fig. 4D proved the differences in compositions. However, the estimated atom fractions of Si and Al by the semi-quantitative XPS analysis were significantly lower than what the EDS results showed, especially for PHZ<sub>4</sub> (at% of Si: 1.38, at% of Al: 1.04). XPS describes the compositions in a very superficial surface due to its shallow detection depth compared with that of EDS; also, as illustrated before, most of the zeolite

particles were covered by the polymer shell. Besides, the high-resolution XPS spectra of PHZ<sub>4</sub> in the range of S 2p and N 1s (Fig. 4E and F) also indicated the presence of PES and P (AA-NVP) in PHZ<sub>4</sub>.

The membrane analogs of the microbeads were prepared for the tests of WCAs and ZPs. WCAs were measured to assess the surface wettability. In Fig. 5A, P and PZ<sub>4</sub> exhibited a hydrophobic nature with WCAs as high as 107.1° and 103.8°, respectively, while the WCA of PH reduced to 51.8° due to the hydrophilic functional groups. The WCA of PHZ<sub>4</sub> dramatically dropped to 0°, even when much lower amounts of zeolite were added (PHZ<sub>0.25</sub> and PHZ<sub>1</sub>, shown in Fig. S6), which indicated a remarkable synergistic effect between the hydrophilic polymer and the zeolite on the enhancement of wettability. ZPs were measured to investigate the charging behavior in contact with aqueous solutions. In Fig. 5B, all the samples were negatively charged and generally became more negative with increasing pH values, owing to the enhanced anion adsorption to the hydrophobic surface of PES at high pH [45]. The samples with the hydrophilic polymer had higher negative values of ZPs compared to the corresponding sample with only PES as the polymer phase (PH to P, and PHZ<sub>4</sub> to PZ<sub>4</sub>) due to the ionization of carboxyl groups. Besides, it might be seemingly paradoxical that the highly ionizable zeolite LTA reduced the negative values of ZPs;

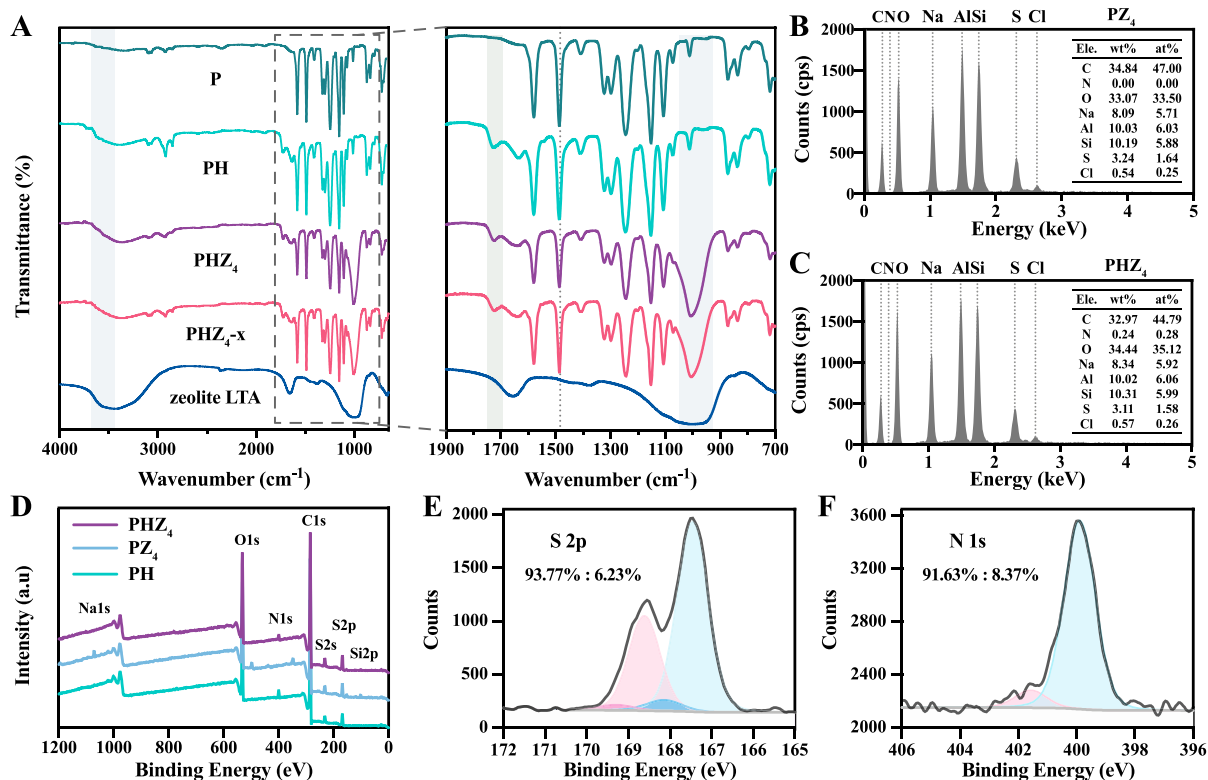


Fig. 4. (A) FTIR spectra of microbeads and zeolite LTA powder. (B–C) EDS results and the calculated mass fractions and the atom fractions of elements in PZ<sub>4</sub> and PHZ<sub>4</sub>. (D) XPS wide scans of the microbeads. (E–F) High-resolution XPS spectra of PHZ<sub>4</sub> in the range of S and N.

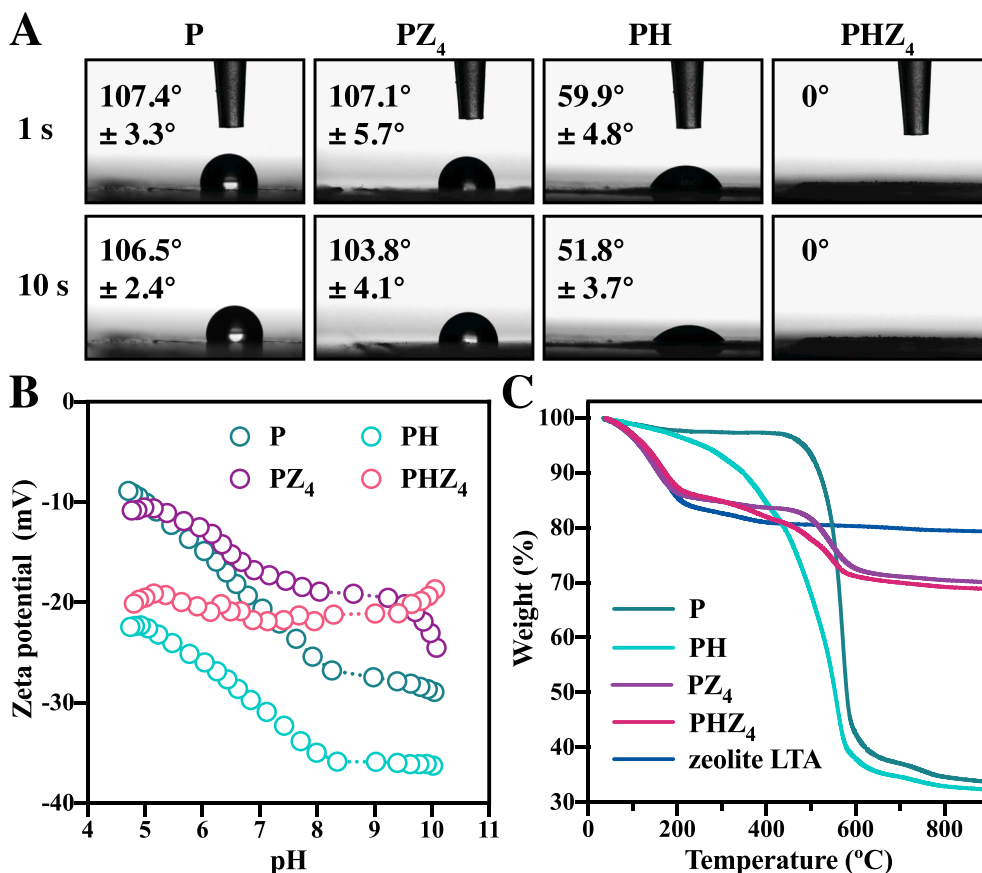


Fig. 5. (A) WCAs of the microbeads at 1 s and 10 s. (B) ZPs of the microbeads at different pH values. (C) TGA curves of the microbeads and zeolite LTA powder.

however, this phenomenon should be attributed to the significant increase in membrane conductivity that affected the streaming currents and thus led to lower measured values than the actual ZPs [46]. Thermal stability and decomposition mechanisms were studied, as shown by the TGA (Fig. 5C) and DTG curves (Fig. S7). The weight loss in zeolite LTA was initiated with the fast dehydration of surface water and then followed the dehydration of the intercrystalline water [47]. The microbeads were thermally stable below 160 °C, and the removal of unbound water was the major weight loss in this stage. In the hybrid microbeads PHZ<sub>4</sub>, the slow weight loss in the range of 160–500 °C was due to the loss of bound water and the decarboxylation of carboxyl groups [47]; the sharp weight loss near 580 °C was due to the degradation of PES; the weight loss slowed down above 650 °C, and the residue was not fully decomposed. The TGA curves of PHZ<sub>4</sub> included the characteristic degradation peaks of each content, albeit with attenuated intensities. The thermal stability of PHZ<sub>4</sub> could meet the temperature demand for the sterilization of biomedical materials in 120–170 °C [48]. The photographs in Fig. S8 shows that the PHZ<sub>4</sub>-x microbeads could soon restore the original shape after compression by weight bars with a total mass of 35 g for 5 min, which indicated sufficient mechanical stability of microbeads to avoid shedding or fragmentation when applied as adsorbents in hemoperfusion treatment.

### 3.4. Potassium uptake

#### 3.4.1. Effect of chemical compositions

The static adsorption tests were conducted to analyze various effects on the K<sup>+</sup> uptake. Fig. 6A shows the K<sup>+</sup> uptake in the microbeads with different chemical compositions. The microbeads P and PH had negligible K<sup>+</sup> uptake, which was because (i) PES had no ionizable groups for ion-exchange; (ii) the anionic P (AA-NVP) had no specific potassium binding ability, while its negatively charged carboxyl groups tended to adsorb the higher-enriched Na<sup>+</sup> or H<sup>+</sup> in normal saline at neutral pH. This affinity to Na<sup>+</sup> by P (AA-NVP) did not decrease K<sup>+</sup> uptake nor

increase Na<sup>+</sup> fluctuation in PHZ<sub>4</sub>. However, PHZ<sub>4</sub> exhibited similar uptake amount with zeolite LTA powder, possibly due to the balance by the carboxylate groups (–COONa) that offset Na<sup>+</sup> fluctuation during adsorption, as before the test the microbeads were immersed in normal saline, where the carboxyl groups (–COOH) were allowed to transform into the carboxylate form.

#### 3.4.2. Effect of zeolite amount

Fig. 6B shows the effect of the added amount of zeolite on the K<sup>+</sup> uptake. The added amounts of zeolite were converted to the mass fractions according to the formulas for hybrid suspensions. The K<sup>+</sup> uptake increased in approximate linearity with zeolite mass fractions, which indicated high added amounts would not reduce the utilization efficiency of zeolite. Therefore, increasing the added amount of zeolite might be a convenient way to improve the K<sup>+</sup> uptake in the microbeads.

#### 3.4.3. Effect of modification method

Fig. 6C shows the effect of the aqueous-phase modification methods on the K<sup>+</sup> uptake. PHZ<sub>4</sub>-DI was set as a control to testify any impact exerted by the process of mixing and heating in deionized water. The almost unchanged uptake in PHZ<sub>4</sub>-Na and PHZ<sub>4</sub>-NH<sub>4</sub>-Na indicated that (i) the ion-exchange modification in the NaCl solution treatment would not affect the K<sup>+</sup> uptake; (ii) the conversion of zeolite from the Na-form to the NH<sub>4</sub>-form could be fully reverted by the subsequent NaCl solution treatment, as verified by Nessler's reagent spectrophotometry. The K<sup>+</sup> uptake increased after metal-leaching modification in acid or an elevated concentration of alkali. The combined methods were adopted for higher K<sup>+</sup> uptake; as expected, the sample PHZ<sub>4</sub>-NH<sub>4</sub>-Acid-Base-Na (PHZ<sub>4</sub>-x) had the highest K<sup>+</sup> uptake, with a 30% increase than the original PHZ<sub>4</sub>. The enhanced accessibility to the internal active sites in zeolite crystals ensured the lower diffusion time and thus the improved K<sup>+</sup> uptake during the adsorption period.

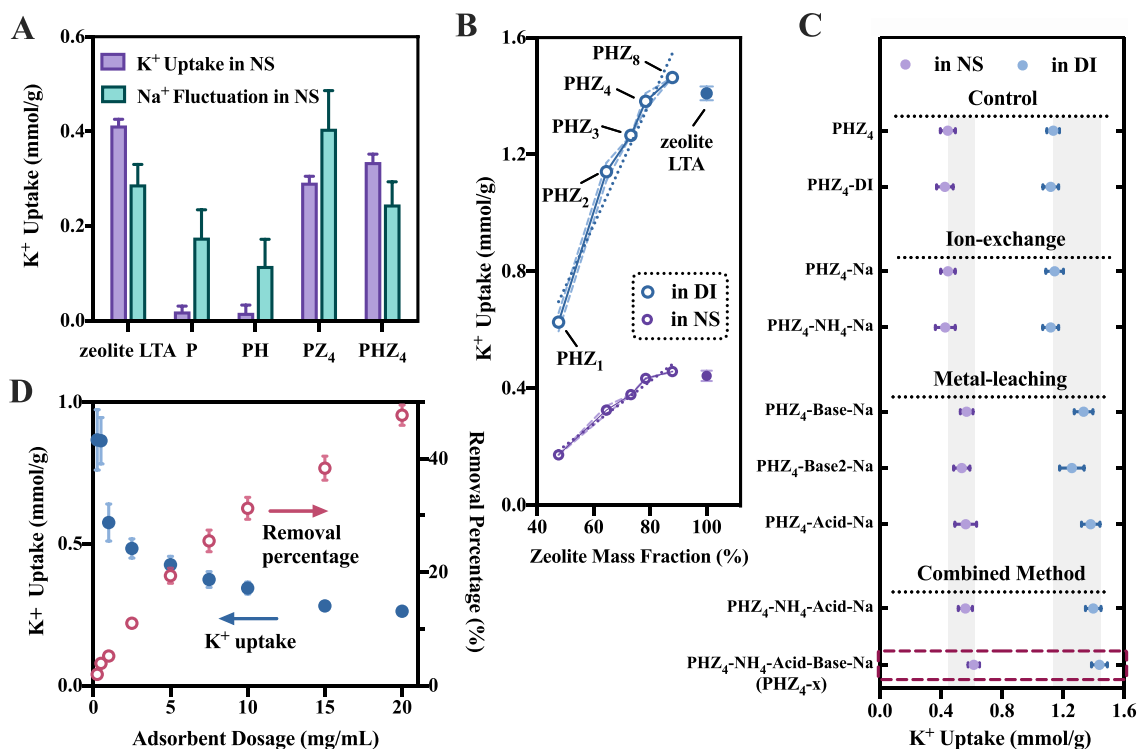
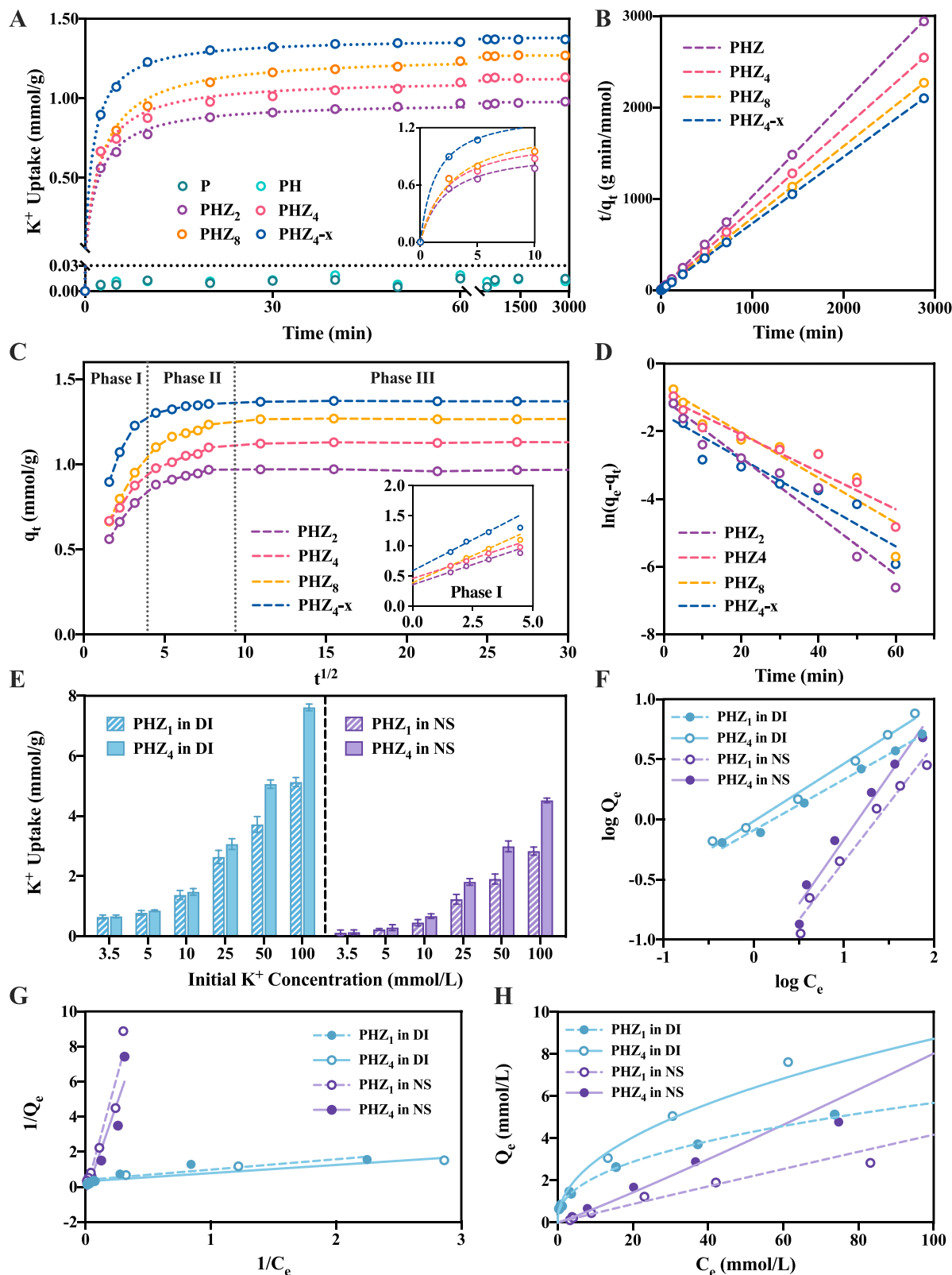


Fig. 6. (A) K<sup>+</sup> uptake and Na<sup>+</sup> fluctuation in the microbeads with different chemical compositions. (B) K<sup>+</sup> uptake in the microbeads with different added amounts of zeolite (at a reduced adsorbent dosage of 2.5 mg/mL). (C) Effect of different modification methods on the K<sup>+</sup> uptake. (D) K<sup>+</sup> uptake and removal percentage of PHZ<sub>4</sub>-x of the NS group at different adsorbent dosages. The results in Fig. 6 were expressed as means ± SD, n = 3.



**Fig. 7.** (A) The scatterplots of the experimental adsorption kinetics, and the fitted curves by the pseudo-second-order kinetic model. (B) The fitted straight lines of the pseudo-second-order kinetic model. (C) The fitted curves of the intraparticle diffusion model for the initial 900 min. (D) The enlarged view of the initial phase of the fitted curves of the intraparticle diffusion model. (E) The  $K^+$  uptake in the microbeads at the varied initial concentrations of  $K^+$ . The results were expressed as means  $\pm$  SD,  $n = 6$ . (F) The Freundlich isotherm plots. (G) The Langmuir isotherm plots. (H) The scatterplots of the experimental adsorption isotherms, and the fitted curves by the Freundlich model.

#### 3.4.4. Effect of adsorbent dosage

Fig. 6D shows the effect of adsorbent dosage on uptake amount and removal percentage in PHZ<sub>4-x</sub> of the NS group. As the dosage increased from 0.25 to 20 mg/mL, the uptake amount per unit mass decreased due to the reduced saturated active sites that were excessive for a lower K<sup>+</sup> concentration; instead, the removal percentage increased from 2% to 48%. The removal percentage did not reach to 100% but about 50% even at a high dosage of 20 mg/mL, which was ascribed to the ion competition from Na<sup>+</sup> that weakened concentration gradients as the driving force, leading to a slow-down in the removal percentage of K<sup>+</sup> and preventing an unexpectedly low K<sup>+</sup> concentration.

#### 3.4.5. Adsorption kinetics

The adsorption kinetics of the microbeads were investigated. As shown in Fig. 7A, the K<sup>+</sup> uptake in P and PH was negligible; the uptake in other hybrid microbeads increased with time before reaching equilibrium. The uptake exceeded 90% of the equilibrium value after a rapid increase in the initial 120 min, indicating fast adsorption; for this reason, the contact time was set at 120 min in other adsorption tests.

The pseudo-first-order and the pseudo-second-order kinetic model (detailed in Supporting Information, Equations S(3) and (4)) were applied to analyze the adsorption kinetics, and the fitting parameters were listed in Table S4. The pseudo-second-order kinetic model was more suitable for the overall adsorption process (within 2880 min), with higher correlation coefficients ( $R^2 > 0.99$ ) than those of the pseudo-first-order kinetic model ( $R^2 < 0.99$ ), which indicated the primary adsorption mechanism followed a fashion of chemical adsorption. The fitted curves by this model are shown in Fig. 7A, and the validity was checked by the fitted straight lines in Fig. 7B. The microbeads with a lower added amount of zeolite showed a lower theoretical equilibrium uptake  $q_e$  and a higher rate constant  $k_2$ , possibly due to improved accessibility for mass diffusion. PHZ<sub>4-x</sub> showed both the highest  $q_e$  and  $k_2$ , which was consistent with its high uptake amount and rate.

The intra-particle diffusion model (detailed in Supporting Information, Equation S(5)) was applied to study the diffusion process. In Fig. 7C, none of the multi-segment lines passed through the origin, which denoted the process was not controlled merely by intra-particle diffusion [49]. Instead, three important phases were involved: (i) the initial phase depicting a fast uptake due to external adsorption associated with macropores and mesopores, during which K<sup>+</sup> transferred across the boundary layer and assembled at the surface of zeolite and polymer; (ii) the subsequent phase with a slope in the line due to intra-particle diffusion associated with micropores, during which K<sup>+</sup> migrated to the channels and cages inside zeolite at a lower diffusion rate; (iii) the final phase of approaching equilibrium with a near plateau, due to the larger occupied active sites and the reduced concentration gradient as a driving force [50,51]. As shown in Fig. 7D, the experimental data of the initial phase (the initial 20 min) were fitted by this model ( $R^2 > 0.9$ ), and the fitting parameters are listed in Table S4. The difference in  $C$  values was insignificant among these samples. PHZ<sub>4-x</sub> had a relatively higher value of  $k_3$ , which indicated a high rate of the initial uptake due to the larger surface areas and active sites [52].

#### 3.4.6. Adsorption isotherms

Fig. 7E shows the effect of the initial K<sup>+</sup> concentrations on the K<sup>+</sup> uptake. The equilibrium uptake in PHZ<sub>1</sub> and PHZ<sub>4</sub> increased with the initial K<sup>+</sup> concentrations in both groups. This uptrend was evident in the NS group, due to the strong ion competition from Na<sup>+</sup> at a low concentration of K<sup>+</sup>, which was gradually weakened by the increasing K<sup>+</sup> concentration. Besides, PHZ<sub>4</sub> had higher uptake than PHZ<sub>1</sub> at any initial K<sup>+</sup> concentrations, due to a higher added amount of zeolite.

The experiment data were analyzed with the Freundlich and Langmuir models (detailed in Supporting Information, Equations S(6) and (7)). The isotherm plots of the Freundlich and Langmuir models were shown in Fig. 7F and G, respectively, and the fitting parameters were listed in Table S5. The Freundlich model fitted the data better,

with higher correlation coefficients, which indicated the K<sup>+</sup> uptake followed a fashion of multilayer adsorption by the heterogeneous surface of the microbeads and by the interactions between the surface and the adsorbed ions [50]. Due to the ion competition from Na<sup>+</sup> of a much higher concentration (155 mmol/L), the microbeads in the NS group generally had lower values of (i) the correlation coefficients ( $0.9 < R^2 < 0.99$ ), which was consistent with the larger deviations of the fitted curves by the Freundlich model, as shown in Fig. 7H; (ii) the Freundlich constants  $n$  and  $k_f$ , denoting the decrease in the adsorption intensity and capacity [52]. Furthermore, these phenomena were evident at the very low initial K<sup>+</sup> concentration of 3.5 mmol/L, the threshold indicating hypokalemia (low serum potassium level). Despite the negative effect on the K<sup>+</sup> uptake, the presence of Na<sup>+</sup> also prevented K<sup>+</sup> from dropping to an unexpectedly low level.

#### 3.4.7. Serum potassium uptake

Since the abundance of various cations, proteins and cells complicated the uptake process in serum, the K<sup>+</sup> uptake in human serum was studied. The serum was isolated from human whole blood and divided into two groups (the normal group and the hyperkalemia group), following the procedures as detailed in Supporting Information.

In the static adsorption test, the levels of serum potassium and sodium were measured at different sampling times after treated with PHZ<sub>4-x</sub> (Fig. 8A). The serum potassium decreased with contacting time but not far below the lower limit of the normal range, and the decrease was more evident in the hyperkalemia group; the serum sodium changed insignificantly within the normal range. Fig. 8B shows the absolute changes in the concentrations of each cation in the hyperkalemia group after treated with the different microbeads. The fluctuations of potassium and sodium were more significant than those of calcium and magnesium. Besides, PHZ<sub>4-x</sub> had the highest K<sup>+</sup> uptake and the lowest Na<sup>+</sup> fluctuation, which was consistent with the uptake results in aqueous solutions. In the column adsorption test, 40 mL of serum for each group was filtered by one column at 37 °C with a flow rate of 15 mL/min, and 1 mL of serum sample was collected after 1–3 cycles. As shown in Fig. 8C, the potassium levels decreased with the increasing cycles down to levels slightly below the normal range, while the sodium level remained normal. The results suggested that the hybrid microbeads exhibited a high efficiency of K<sup>+</sup> uptake when applied in human serum, as well as the prospect as the column adsorbent utilized in the hemoperfusion treatment for hyperkalemia. Fig. 8D shows the miniature column prepared for the hemoperfusion simulation. The hybrid microbeads PHZ<sub>4-x</sub> were packed in a syringe tube at a volume of 2 mL, with each piece of Nylon mesh filter at the top and the bottom of the column to hold the shape. Fig. 8E displays the unit cell of the hydrated Na-LTA crystal encircled by potassium ions and the {1 0 0} surface of the dehydrated Na-LTA. Since the full conversion to the Na-form during modifications (Figs. S2–4), the structure of zeolite LTA in PHZ<sub>4-x</sub> was depicted as the unit cell of the hydrated Na-LTA. The high-aluminum content (Si/Al ratio = ~1, Fig. 4C) ensured sufficient hydration of the extraframework Na<sup>+</sup> ions, leading to high hydrophilicity (Fig. 5A). The free K<sup>+</sup> ions with an ionic radius of 1.38 Å could readily diffuse across the 8-ring windows of 4 Å and the 6-ring windows of 2.5 Å, preferentially exchangeable for the Na<sup>+</sup> ions (Figs. 6–8) [53]. The serum potassium uptake resulted from the balance established by the multiple conversions of LTA (Na-LTA to K/Ca/Mg-LTA) based on ion competition.

### 3.5. Blood compatibility

#### 3.5.1. Protein adsorption

Protein fouling reduces water permeability and provides a layer for microbial colonization, and it is also associated with the adhesion and activation of cells, resulting in a high risk of thrombosis once PLTs are deposited and activated [54,55]. Two proteins, BSA and BFG, were applied in the static protein adsorption tests. In Fig. 9A, the microbeads

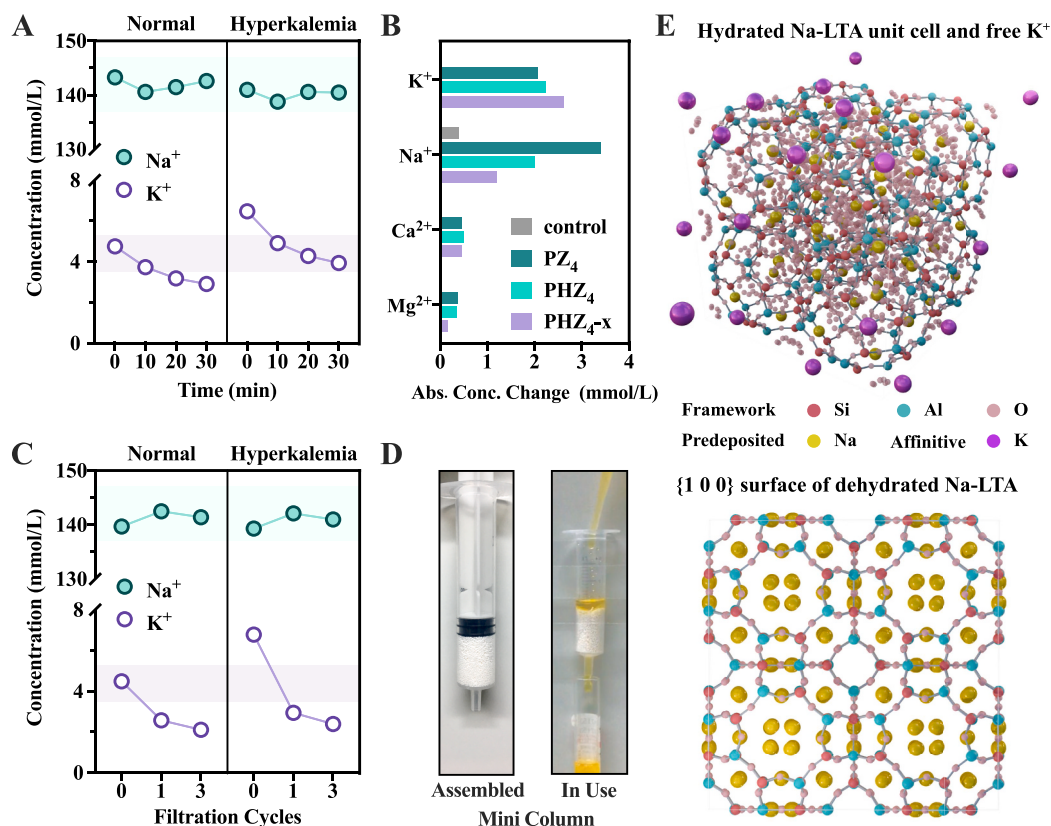


**Fig. 8.** (A) Levels of serum potassium and sodium at different sampling times when treated with PHZ<sub>4-x</sub>. (B) Absolute changes in the concentration of each serum cation in the hyperkalemia group after treated with different microbeads with normal serum as a control. (C) Levels of serum potassium and sodium after different filtration cycles when treated with PHZ<sub>4-x</sub> in the column test. The background of a light green or purple represents the normal serum sodium or potassium, respectively. (D) Photographs of the miniature column packed with PHZ<sub>4-x</sub> for the hemoperfusion simulation. (E) The unit cell of the hydrated Na-LTA crystal encircled by potassium ions, and the {1 0 0} surface of the dehydrated Na-LTA.

PH showed lower adsorption amounts of both proteins than P due to enhanced hydrophilicity [42]. The hybrid microbeads with an ultra-high amount of zeolite were assumed to have higher protein adsorption amounts due to larger surface areas. However, the microbeads with zeolite had even lower protein adsorption amounts than did PH. The possible reasons were as follows: (i) the zeolite particles mostly located inside the microbeads (as shown in Fig. 3); (ii) zeolite LTA introduced electrostatic repulsion with the same negatively charged proteins (as shown by ZPs, Fig. 5B), and also provided super hydrophilicity and abundant framework oxygen atoms as hydrogen-bond acceptors, which fulfilled the “Whitesides rules” and hence suppressed protein adsorption [56,57]. The effect of different aqueous-phase modification methods on protein adsorption was evaluated. As shown in Fig. 9B, the microbeads treated by the metal-leaching process generally had enhanced antifouling property compared to the original PHZ<sub>4</sub>, while those treated with only the ion-exchange process showed insignificant improvement.

### 3.5.2. Blood routine

The blood routine test further analyzed the hemocyte compatibility of the blood-contacting materials. In Fig. S9, there was no noticeable change in the volume distributions of RBCs and PLTs in the microbeads compared with the control. In Fig. 9C, the microbead PHZ<sub>4-x</sub> had similar cell counts with the control, which indicated insignificant effects on the hemocytes exerted by the microbeads and also reflected an advantage over zeolite LTA powder in contact with blood.

### 3.5.3. Complement activation, contact activation and platelet activation

The concentrations of C3a and C5a were measured to detect the

complement activation level [64]. In Fig. 9D, the results showed no significant changes in the concentrations of C3a and C5a compared with the whole blood, which indicated the microbeads would not trigger complement activation. The concentration of TAT and PF4 were measured to evaluate the levels of contact activation and platelet activation. All the microbeads except P had a significantly lower concentration of TAT than the whole blood. Besides, the introduction of zeolite further contributed to decreasing TAT concentrations, which might be ascribed to the anticoagulant property of the microbeads [65]. The hybrid microbeads treated with the metal-leaching process had a 35% and 50% reduction in the concentrations of TAT and PF4, respectively, indicating suppressed thrombin generation and platelet adhesion [66].

### 3.5.4. Platelet adhesion

The resistance to platelet adhesion in the microbeads was investigated, as the adhesion of PLTs would lead to further activation and aggregation [58]. The representative SEM images of the adhered PLTs on the microbead surface are shown in Fig. 10A, and the estimated amounts of the adhered PLTs and RBCs are shown in Fig. S10. On the surface of P scattered many PLTs; some of them were activated, with deformation and pseudopodia. On the surface of PH, the adhered PLTs were fewer in number and more intact in shape; the resistance to platelet adhesion was more notable in the hybrid microbeads of zeolite.

### 3.5.5. Hemolysis

Hemolysis is related to hemoglobin release, platelet activation and thrombus formation; it leads to an elevated potassium level as the release of intracellular potassium into the serum [59]. As shown in Fig.

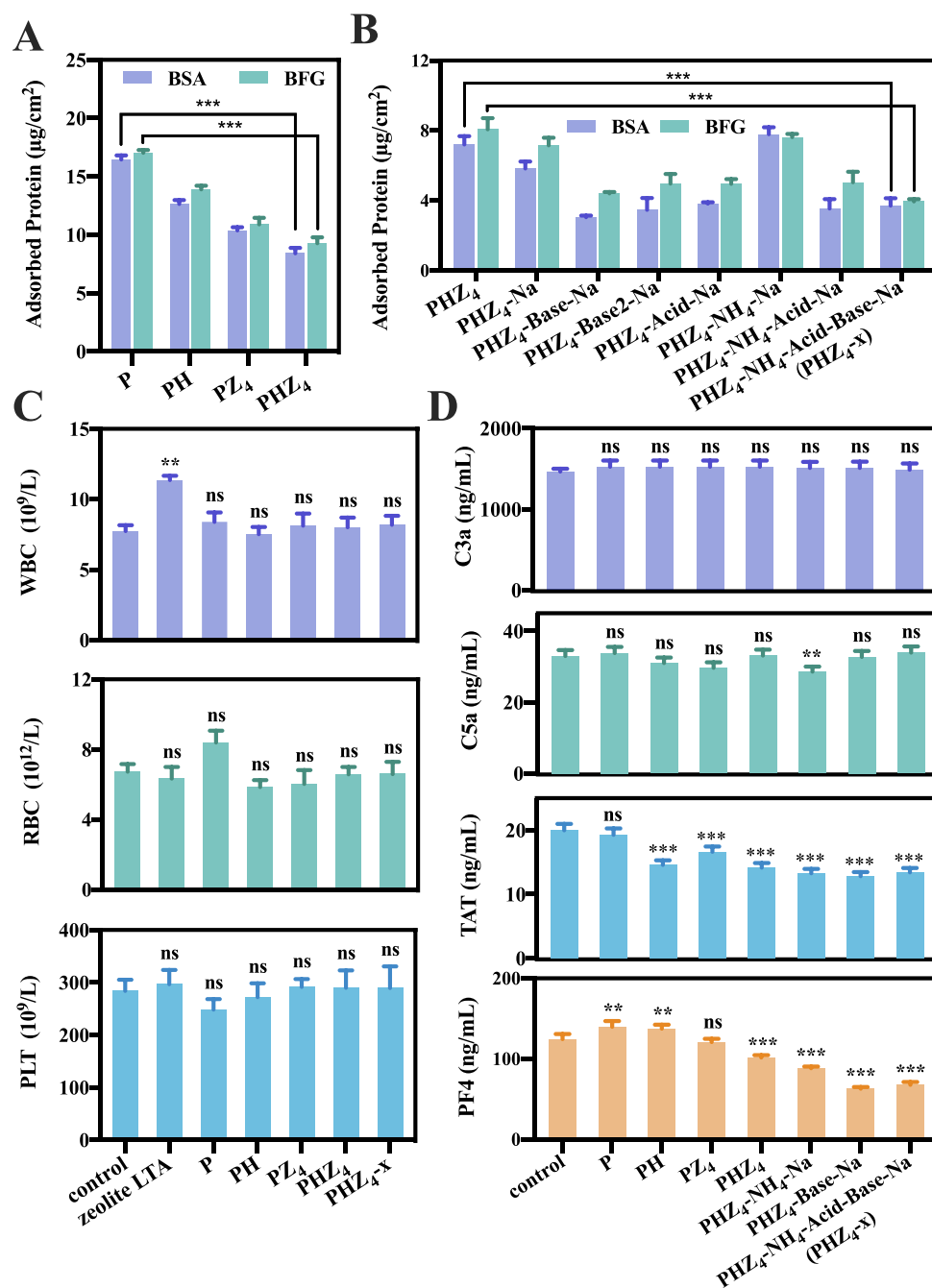


**Fig. 9.** (A) Effect of chemical compositions and (B) aqueous-phase modification methods on protein adsorption for the microbeads. The results were expressed as means  $\pm$  SD,  $n = 6$ . (C) Counts of WBCs, RBCs and PLTs in the blood sample after incubation with microbeads or zeolite powder. (D) Levels of complement activation, contact activation and platelet activation of the microbeads. The results were expressed as means  $\pm$  SD,  $n = 3$ . \*\*\* represents very significant changes ( $***P < 0.001$ ), \*\* represents significant changes ( $0.01 < **P < 0.001$ ), and ns represents no significant changes ( $P > 0.05$ ).

S11, the microbeads exhibited much lower hemolysis rates ( $< 0.5\%$ ) than the permissible level ( $< 5\%$ ) [60]. Compared with P, the slight increase in the hemolysis rate of PH was due to the carboxyl groups, which could be offset by the added zeolite and the aqueous-phase modifications, resulting in a very low hemolysis rate in PHZ<sub>4</sub>-x. Besides, the supernatants remained transparent and colorless, indicating a negligible amount of hemoglobin released by hemolysis. As shown in Fig. 10B, the adhered RBCs on the surface of PHZ<sub>4</sub>-x exhibited the typical biconcave disc shape and a reduced amount. The optical microscopic images in Fig. 10C display the morphologies of RBCs sampled from the suspensions incubated with the microbeads. The RBCs in these samples had a distinct outline with perfect circularity, while only

ruptured RBCs in a red background could be seen in the positive control. As shown by the schematic drawings in Fig. 10D, the hybrid microbeads benefited from the heparin-mimicking polymer and exhibited improved compatibility in contact with RBCs and PLTs.

### 3.5.6. Clotting time

The anticoagulant properties were investigated by the clotting time test, as shown in Fig. S12. These samples had insignificant prolongation of PT and TT over PPP. However, APTT increased in all these microbeads except the original P, and the prolongation of APTT was most significant in PHZ<sub>4</sub>-x (63.9 s), which indicated the inhibition of intrinsic and common coagulation pathway [61]. It could be due to several

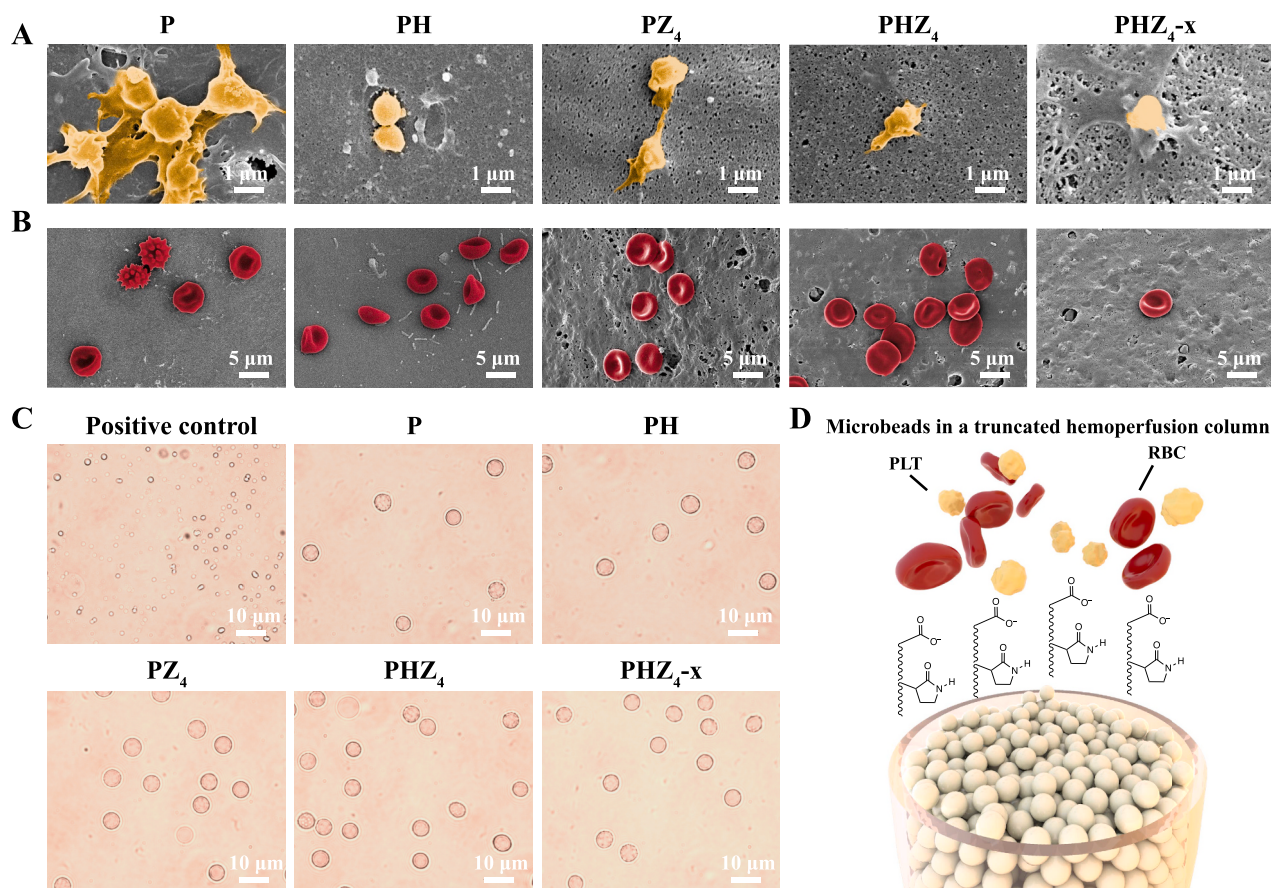


**Fig. 10.** (A) SEM images of PLTs and (B) RBCs adhered to the surface of the microbeads. (C) Optical microscopic images of RBCs sampled from the suspensions. (D) Schematic drawings of the microbeads with the functional groups as the adsorbent in a hemoperfusion column in contact with RBCs and PLTs.

reasons: (i) the reduced protein adsorption amount, and (ii) the carboxylate groups and the zeolite that bound  $\text{Ca}^{2+}$  to inhibit the activation of Factor IX, Factor X and prothrombin [62,63].

#### 4. Conclusions

We explored the efficacy of the zeolite–polymer hybrids microbeads in potassium uptake and the potential application in blood purification. A commercially-available super-hydrophilic LTA-type zeolite was selected from the six binding agents. The heparin-mimicking polymer was prepared via the *in situ* cross-linking polymerization and served as the cross-linked matrix to lock the ultra-high amount of zeolite. Systematic characterizations verified the synthesis and modifications. Adsorption tests confirmed the potassium uptake, along with high selectivity and fast kinetics in water, normal saline and human serum. The microbeads exhibited satisfying blood compatibility, with enhanced adsorption resistance toward serum proteins ( $< 4 \mu\text{g}/\text{cm}^2$  for BSA/BFG adsorption) and cells ( $> 80\%$  reduction for adhered RBCs/PLTs), negligible hemolysis rates ( $< 0.5\%$ ), prolonged clotting time (64.9 s for APTT), and inhibition of contact activation and platelet activation (35% and 50% reduction for TAT and PF4). Conclusively, the microbeads had great potential in blood purification, as a cheap, efficient and safe alternative for hyperkalemia treatment.

##### 4.1. Human subjects

This experiment conformed to the legal requirement in China and was approved by the ethical committee (No. 2020172A) of West China Hospital, Sichuan University.

#### CRediT authorship contribution statement

**Zhoujun Wang:** Investigation, Formal analysis, Visualization, Writing - original draft. **Wei Sun:** Resources. **Zhiwei Wei:** Visualization. **Jianxu Bao:** Validation. **Xin Song:** Writing - review & editing. **Yupei Li:** Writing - review & editing. **Haifeng Ji:** Methodology. **Jue Zhang:** Methodology. **Chao He:** Resources. **Baihai Su:** Resources. **Weifeng Zhao:** Conceptualization, Project administration. **Changsheng Zhao:** Supervision.

#### Declaration of competing interest

The authors declare no conflict of interest regarding the publication of this article.

#### Acknowledgments

This work was financially sponsored by the State Key Research Development Programme of China (Grant No. 2016YFC1103000), the National Natural Science Foundation of China (No. 51773127, 51873115) and Science and Technology Program of Sichuan Province (2019YJ0132). We gratefully acknowledge the help of the Analytical and Testing Center at Sichuan University for the SEM and XPS analysis.

#### Appendix A. Supplementary data

Supplementary data to this article can be found online at <https://doi.org/10.1016/j.bioactmat.2020.08.032>.

## References

- [1] J.R. Ingelfinger, A new era for the treatment of hyperkalemia? *N. Engl. J. Med.* 372 (2014) 275–277, <https://doi.org/10.1056/NEJMe1414112>.
- [2] S.L. Seliger, Hyperkalemia in patients with chronic renal failure, *Nephrol. Dial. Transplant.* 34 (2019) iii12–iii18, <https://doi.org/10.1093/ndt/gfz231>.
- [3] M.A. Pfeffer, E.A. Burdman, C.-Y. Chen, M.E. Cooper, D. de Zeeuw, K.-U. Eckardt, J.M. Feysi, P. Ivanovich, R. Kewalramani, A.S. Levey, E.F. Lewis, J.B. McGill, J.J.V. McMurray, P. Parfrey, H.-H. Parving, G. Remuzzi, A.K. Singh, S.D. Solomon, R. Toto, A trial of darbepoetin alfa in type 2 diabetes and chronic kidney disease, *N. Engl. J. Med.* 361 (2009) 2019–2032, <https://doi.org/10.1056/NEJMoa0907845>.
- [4] B.F. Palmer, Managing hyperkalemia caused by inhibitors of the renin–angiotensin–aldosterone system, *N. Engl. J. Med.* 351 (2004) 585–592, <https://doi.org/10.1056/NEJMra035279>.
- [5] M.L. Gumz, L. Rabinowitz, C.S. Wingo, An integrated view of potassium homeostasis, *N. Engl. J. Med.* 373 (2015) 60–72, <https://doi.org/10.1056/NEJMra1313341>.
- [6] A. Karaboyas, J. Zee, S.M. Brunelli, L.A. Usvyat, D.E. Weiner, F.W. Maddux, A.R. Nissenson, M. Jadoul, F. Locatelli, W.C. Winkelmayer, F.K. Port, B.M. Robinson, F. Tentori, Dialysate potassium, serum potassium, mortality, and arrhythmia events in hemodialysis: Results from the dialysis outcomes and practice patterns study (DOPPS), *Am. J. Kidney Dis.* 69 (2017) 266–277, <https://doi.org/10.1053/j.ajkd.2016.09.015>.
- [7] A.M. Hung, R.M. Hakim, Dialysate and serum potassium in hemodialysis, *Am. J. Kidney Dis.* 66 (2015) 125–132, <https://doi.org/10.1053/j.ajkd.2015.02.322>.
- [8] V. Gura, A. Davenport, M. Beizai, C. Ezon, C. Ronco,  $\beta$ 2-Microglobulin and phosphate clearances using a wearable artificial kidney: A pilot study, *Am. J. Kidney Dis.* 54 (2009) 104–111, <https://doi.org/10.1053/j.ajkd.2009.02.006>.
- [9] A.K.S. Clemens, A. Shishkin, P.-A. Carlsson, M. Skoglundh, F.J. Martínez-Casado, Z. Matěj, O. Balmes, H. Härelind, Reaction-driven ion exchange of copper into zeolite SSZ-13, *ACS Catal.* 5 (2015) 6209–6218, <https://doi.org/10.1021/acscatal.5b01200>.
- [10] A. Mayoral, T. Carey, P.A. Anderson, A. Lubk, I. Diaz, Atomic resolution analysis of silver ion-exchanged Zeolite A, *Angew. Chem. Int. Ed.* 50 (2011) 11230–11233, <https://doi.org/10.1002/anie.201105450>.
- [11] X. Guo, L. Zeng, X. Li, H.-S. Park, Ammonium and potassium removal for anaerobically digested wastewater using natural clinoptilolite followed by membrane pretreatment, *J. Hazard Mater.* 151 (2008) 125–133, <https://doi.org/10.1016/j.jhazmat.2007.05.066>.
- [12] D.K. Packham, H.S. Rasmussen, P.T. Lavin, M.A. El-Shahawy, S.D. Roger, G. Block, W. Qunibi, P. Pergola, B. Singh, Sodium zirconium cyclosilicate in hyperkalemia, *N. Engl. J. Med.* 372 (2014) 222–231, <https://doi.org/10.1056/NEJMoa1411487>.
- [13] Y. Cheng, X. Dong, S. Jaenicke Tony) Wang, G.-K. Chuah, Mechanochemistry-based synthesis of highly crystalline  $\gamma$ -zirconium phosphate for selective ion exchange, *Inorg. Chem.* 57 (2018) 4370–4378, <https://doi.org/10.1021/acs.inorgchem.7b03202>.
- [14] T. Takei, K. Aoyama, S. Yanagida, N. Kumada, Y. Nakajima, Circumstances of La, Eu, Dy, and Yb cations intercalated via ion exchange in  $\gamma$ -zirconium phosphate, *Inorg. Chem.* 57 (2018) 13097–13103, <https://doi.org/10.1021/acs.inorgchem.8b01003>.
- [15] Y. Wang, Z. Wang, Y. Chen, H. Zhang, M. Yousaf, H. Wu, M. Zou, A. Cao, R.P.S. Han, Hyperporous sponge interconnected by hierarchical carbon nanotubes as a high-performance potassium-ion battery anode, *Adv. Mater.* 30 (2018) 1802074, <https://doi.org/10.1002/adma.201802074>.
- [16] M. Chen, W. Wang, X. Liang, S. Gong, J. Liu, Q. Wang, S. Guo, H. Yang, Sulfur/oxygen codoped porous hard carbon microspheres for high-performance potassium-ion batteries, *Adv. Energy Mater.* 8 (2018) 1800171, <https://doi.org/10.1002/aenm.201800171>.
- [17] G.M. Böglés, J.A.M. Lügger, O.J.G.M. Goor, R.P. Sijbesma, Size-selective binding of sodium and potassium ions in nanoporous thin films of polymerized liquid crystals, *Adv. Funct. Mater.* 26 (2016) 8023–8030, <https://doi.org/10.1002/adfm.201603408>.
- [18] Y. Huang, W. Zhao, X. Zhang, H. Peng, Y. Gong, Thiol-ene synthesis of thioether/carboxyl-functionalized polymers for selective adsorption of silver (I) ions, *Chem. Eng. J.* 375 (2019) 121935, <https://doi.org/10.1016/j.cej.2019.121935>.
- [19] J. Qiu, Y. Zhang, C. Dong, Y. Huang, L. Sun, H. Ruan, H. Wang, X. Li, A. Wu, Rapid colorimetric detection of potassium ions based on crown ether modified Au NPs sensor, *Sens. Actuator. B Chem.* 281 (2019) 783–788, <https://doi.org/10.1016/j.snb.2018.10.139>.
- [20] H.-R. Yu, X.-J. Ju, R. Xie, W. Wang, B. Zhang, L.-Y. Chu, Portable diagnosis method of hyperkalemia using potassium-recognizable poly(N-isopropylacrylamide-co-benzo-15-crown-5-acrylamide) copolymers, *Anal. Chem.* 85 (2013) 6477–6484, <https://doi.org/10.1021/ac401028a>.
- [21] A. Fang, K. Kroenlein, D. Riccardi, A. Smolyanitsky, Highly mechanosensitive ion channels from graphene-embedded crown ethers, *Nat. Mater.* 18 (2019) 76–81, <https://doi.org/10.1038/s41563-018-0220-4>.
- [22] A. Smolyanitsky, E. Paulechka, K. Kroenlein, Aqueous ion trapping and transport in graphene-embedded 18-crown-6 ether pores, *ACS Nano* 12 (2018) 6677–6684, <https://doi.org/10.1021/acsnano.8b01692>.
- [23] C. Baerlocher, L.B. McCusker, D.H. Olson, *Atlas of Zeolite Framework Types*, Elsevier, 2007.
- [24] B. Smit, T.L.M. Maesen, Molecular simulations of zeolites: adsorption, diffusion, and shape selectivity, *Chem. Rev.* 108 (2008) 4125–4184, <https://doi.org/10.1021/cr8002642>.
- [25] K. Möller, T. Bein, Mesoporosity – a new dimension for zeolites, *Chem. Soc. Rev.* 42 (2013) 3689–3707, <https://doi.org/10.1039/C3CS35488A>.
- [26] H. Liu, S. Peng, L. Shu, T. Chen, T. Bao, R.L. Frost, Effect of Fe3O4 addition on removal of ammonium by zeolite NaA, *J. Colloid Interface Sci.* 390 (2013) 204–210, <https://doi.org/10.1016/j.jcis.2012.09.010>.
- [27] K. Namekawa, M. Tokoro Schreiber, T. Aoyagi, M. Ebara, Fabrication of zeolite–polymer composite nanofibers for removal of uremic toxins from kidney failure patients, *Biomater. Sci.* 2 (2014) 674–679, <https://doi.org/10.1039/C3BM60263J>.
- [28] K.L.M. Taaca, M.R. Vasquez, Hemocompatibility and cytocompatibility of pristine and plasma-treated silver-zeolite-chitosan composites, *Appl. Surf. Sci.* 432 (2018) 324–331, <https://doi.org/10.1016/j.apsusc.2017.04.034>.
- [29] Y. Feng, Y. Wang, Y. Wang, S. Liu, J. Jiang, C. Cao, J. Yao, Simple fabrication of easy handling millimeter-sized porous attapulgite/polymer beads for heavy metal removal, *J. Colloid Interface Sci.* 502 (2017) 52–58, <https://doi.org/10.1016/j.jcis.2017.04.086>.
- [30] Y. Yang, P. Gao, J. Wang, Q. Tu, L. Bai, K. Xiong, H. Qiu, X. Zhao, M.F. Maitz, H. Wang, X. Li, Q. Zhao, Y. Xiao, N. Huang, Z. Yang, Endothelium-mimicking multifunctional coating modified cardiovascular stents via a stepwise metal-catechol(amine) surface engineering strategy, *Research* 2020 (2020) 9203906.
- [31] J. Hou, Y. Pan, D. Zhu, Y. Fan, G. Feng, Y. Wei, H. Wang, K. Qin, T. Zhao, Q. Yang, Y. Zhu, Y. Che, Y. Liu, J. Cheng, D. Kong, P.G. Wang, J. Shen, Q. Zhao, Targeted delivery of nitric oxide via a ‘bump-and-hole’-based enzyme–prodrug pair, *Nat. Chem. Biol.* 15 (2019) 151–160, <https://doi.org/10.1038/s41589-018-0190-5>.
- [32] S.-S. Li, Y. Xie, T. Xiang, L. Ma, C. He, S. Sun, C.-S. Zhao, Heparin-mimicking polyethersulfone membranes – hemocompatibility, cytocompatibility, antifouling and antibacterial properties, *J. Membr. Sci.* 498 (2016) 135–146, <https://doi.org/10.1016/j.memsci.2015.09.054>.
- [33] J. Zhang, Z. Shi, C. He, X. Song, Y. Yang, S. Sun, W. Zhao, C. Zhao, Urease immobilized GO core@shell heparin-mimicking polymer beads with safe and effective urea removal for blood purification, *Int. J. Biol. Macromol.* 156 (2020) 1503–1511, <https://doi.org/10.1016/j.ijbiomac.2019.11.197>.
- [34] J.I. Shen, W.C. Winkelmayer, Use and safety of unfractionated heparin for anticoagulation during maintenance hemodialysis, *Am. J. Kidney Dis.* 60 (2012) 473–486, <https://doi.org/10.1053/j.ajkd.2012.03.017>.
- [35] G. Chen, Y. Wang, H. Weng, Z. Wu, K. He, P. Zhang, Z. Guo, M. Lin, Selective separation of Pd(II) on pyridine-functionalized graphene oxide prepared by radiation-induced simultaneous grafting polymerization and reduction, *ACS Appl. Mater. Interfaces* 11 (2019) 24560–24570, <https://doi.org/10.1021/acsaami.9b06162>.
- [36] C. Cheng, S. Sun, C. Zhao, Progress in heparin and heparin-like/mimicking polymer-functionalized biomedical membranes, *J. Mater. Chem. B* 2 (2014) 7649–7672, <https://doi.org/10.1039/C4TB01390E>.
- [37] S. Turgman-Cohen, J.C. Araque, E.M.V. Hoek, F.A. Escobedo, Molecular dynamics of equilibrium and pressure-driven transport properties of water through LTA-type zeolites, *Langmuir* 29 (2013) 12389–12399, <https://doi.org/10.1021/la402895h>.
- [38] S. Calero, P. Gómez-Álvarez, Effect of the confinement and presence of cations on hydrogen bonding of water in LTA-type zeolite, *J. Phys. Chem. C* 118 (2014) 9056–9065, <https://doi.org/10.1021/jp5014847>.
- [39] W. Greñ, S.C. Parker, B. Slater, D.W. Lewis, Structure of zeolite A (LTA) surfaces and the zeolite A/water interface, *J. Phys. Chem. C* 114 (2010) 9739–9747, <https://doi.org/10.1021/jp909355e>.
- [40] J. Pérez-Ramírez, D. Verboekend, A. Bonilla, S. Abelló, Zeolite catalysts with tunable hierarchy factor by pore-growth moderators, *Adv. Funct. Mater.* 19 (2009) 3972–3979, <https://doi.org/10.1002/adfm.200901394>.
- [41] Y. Tao, H. Kanoh, L. Abrams, K. Kaneko, Mesopore-modified Zeolites: preparation, characterization, and applications, *Chem. Rev.* 106 (2006) 896–910, <https://doi.org/10.1021/cr040204o>.
- [42] H.-F. Ji, C. He, R. Wang, X. Fan, L. Xiong, W.-F. Zhao, C.-S. Zhao, Multifunctionalized polyethersulfone membranes with networked submicrogels to improve antifouling property, antibacterial adhesion and blood compatibility, *Mater. Sci. Eng. C* 96 (2019) 402–411, <https://doi.org/10.1016/j.msec.2018.11.047>.
- [43] M. Król, J. Minkiewicz, W. Mozgawa, IR spectroscopy studies of zeolites in geopolymeric materials derived from kaolinite, *J. Mol. Struct.* 1126 (2016) 200–206, <https://doi.org/10.1016/j.jmolstruc.2016.02.027>.
- [44] M. Gackowski, K. Tarach, Ł. Kuterasiński, J. Podobiński, B. Sulikowski, J. Datka, Spectroscopic IR and NMR studies of hierarchical zeolites obtained by desilication of zeolite Y: optimization of the desilication route, *Microporous Mesoporous Mater.* 281 (2019) 134–141, <https://doi.org/10.1016/j.micromeso.2019.03.004>.
- [45] R. Zimmermann, U. Freudenberg, R. Schweiß, D. Küttner, C. Werner, Hydroxide and hydronium ion adsorption – A survey, *Curr. Opin. Colloid Interface Sci.* 15 (2010) 196–202, <https://doi.org/10.1016/j.cocis.2010.01.002>.
- [46] H. Xie, T. Saito, M.A. Hickner, Zeta potential of ion-conductive membranes by streaming current measurements, *Langmuir* 27 (2011) 4721–4727, <https://doi.org/10.1021/la105120f>.
- [47] P. Sharma, J.-S. Song, M.H. Han, C.-H. Cho, GIS-NaP1 zeolite microspheres as potential water adsorption material: Influence of initial silica concentration on adsorptive and physical/topological properties, *Sci. Rep.* 6 (2016) 22734, <https://doi.org/10.1038/srep22734>.
- [48] F. Tessarolo, G. Nollo, Sterilization of biomedical materials, *Encycl. Biomater. Biomed. Eng.* 2016 (2008) 2501–2510.
- [49] K. Rida, S. Bouraoui, S. Hadnine, Adsorption of methylene blue from aqueous solution by kaolin and zeolite, *Appl. Clay Sci.* 83–84 (2013) 99–105, <https://doi.org/10.1016/j.clay.2013.08.015>.
- [50] K. Wang, F. Wang, F. Chen, X. Cui, Y. Wei, L. Shao, M. Yu, One-pot preparation of NaA zeolite microspheres for highly selective and continuous removal of Sr(II) from aqueous solution, *ACS Sustain. Chem. Eng.* 7 (2019) 2459–2470, <https://doi.org/10.1021/acssuschemeng.8b05349>.

- [51] A.E. Ofomaja, Kinetic study and sorption mechanism of methylene blue and methyl violet onto mansonia (*Mansonia altissima*) wood sawdust, *Chem. Eng. J.* 143 (2008) 85–95, <https://doi.org/10.1016/j.cej.2007.12.019>.
- [52] Y. Li, Q. Du, T. Liu, J. Sun, Y. Jiao, Y. Xia, L. Xia, Z. Wang, W. Zhang, K. Wang, H. Zhu, D. Wu, Equilibrium, kinetic and thermodynamic studies on the adsorption of phenol onto graphene, *Mater. Res. Bull.* 47 (2012) 1898–1904, <https://doi.org/10.1016/j.materresbull.2012.04.021>.
- [53] S.M. Auerbach, K.A. Carrado, P.K. Dutta, *Handbook of Zeolite Science and Technology*, CRC press, 2003.
- [54] I. Banerjee, R.C. Pangule, R.S. Kane, Antifouling coatings: Recent developments in the design of surfaces that prevent fouling by proteins, bacteria, and marine organisms, *Adv. Mater.* 23 (2011) 690–718, <https://doi.org/10.1002/adma.201001215>.
- [55] Q. Da, M. Teruya, P. Guchhait, J. Teruya, J.S. Olson, M.A. Cruz, Free hemoglobin increases von Willebrand factor-mediated platelet adhesion in vitro: Implications for circulatory devices, *Blood* 126 (2015) 2338–2341, <https://doi.org/10.1182/blood-2015-05-648030>.
- [56] Q. Wei, T. Becherer, S. Angioletti-Uberti, J. Dzubiella, C. Wischke, A.T. Neffe, A. Lendlein, M. Ballauff, R. Haag, Protein interactions with polymer coatings and biomaterials, *Angew. Chem. Int. Ed.* 53 (2014) 8004–8031, <https://doi.org/10.1002/anie.201400546>.
- [57] R.G. Chapman, E. Ostuni, S. Takayama, R.E. Holmlin, L. Yan, G.M. Whitesides, Surveying for surfaces that resist the adsorption of proteins, *J. Am. Chem. Soc.* 122 (2000) 8303–8304, <https://doi.org/10.1021/ja000774f>.
- [58] N. Mackman, Triggers, targets and treatments for thrombosis, *Nature* 451 (2008) 914–918, <https://doi.org/10.1038/nature06797>.
- [59] H. Fan, P. Chen, R. Qi, J. Zhai, J. Wang, L. Chen, L. Chen, Q. Sun, Y. Song, D. Han, L. Jiang, Greatly improved blood compatibility by microscopic multiscale design of surface architectures, *Small* 5 (2009) 2144–2148, <https://doi.org/10.1002/smll.200900345>.
- [60] ASTM-F756-08, *Standard Practice for Assessment of Hemolytic Properties of Materials*, (2008).
- [61] S. Nie, M. Tang, C. Cheng, Z. Yin, L. Wang, S. Sun, C. Zhao, Biologically inspired membrane design with a heparin-like interface: prolonged blood coagulation, inhibited complement activation, and bio-artificial liver related cell proliferation, *Biomater. Sci.* 2 (2014) 98–109, <https://doi.org/10.1039/C3BM60165J>.
- [62] H. Qin, C. Sun, C. He, D. Wang, C. Cheng, S. Nie, S. Sun, C. Zhao, High efficient protocol for the modification of polyethersulfone membranes with anticoagulant and antifouling properties via in situ cross-linked copolymerization, *J. Membr. Sci.* 468 (2014) 172–183, <https://doi.org/10.1016/j.memsci.2014.06.006>.
- [63] M. He, Q. Wang, R. Wang, Y. Xie, W. Zhao, C. Zhao, Design of antibacterial poly (ether sulfone) membranes via covalently attaching hydrogel thin layers loaded with Ag nanoparticles, *ACS Appl. Mater. Interfaces* 9 (2017) 15962–15974, <https://doi.org/10.1021/acsami.7b03176>.
- [64] A.E. Engberg, P.H. Nilsson, S. Huang, K. Fromell, O.A. Hamad, T.E. Mollnes, J.P. Rosengren-Holmberg, K. Sandholm, Y. Teramura, I.A. Nicholls, B. Nilsson, K.N. Ekdahl, Prediction of inflammatory responses induced by biomaterials in contact with human blood using protein fingerprint from plasma, *Biomaterials* 36 (2015) 55–65, <https://doi.org/10.1016/j.biomaterials.2014.09.011>.
- [65] X. Song, T. Xu, L. Yang, Y. Li, Y. Yang, L. Jin, J. Zhang, R. Zhong, S. Sun, W. Zhao, C. Zhao, Self-anticoagulant nanocomposite spheres for the removal of bilirubin from whole blood: A step toward a wearable artificial liver, *Biomacromolecules* 21 (2020) 1762–1775, <https://doi.org/10.1021/acs.biomac.9b01686>.
- [66] X. Song, K. Wang, C.-Q. Tang, W.-W. Yang, W.-F. Zhao, C.-S. Zhao, Design of carageenan-based heparin-mimetic gel beads as self-anticoagulant hemoperfusion adsorbents, *Biomacromolecules* 19 (2018) 1966–1978, <https://doi.org/10.1021/acs.biomac.7b01724>.